

Mapping Interstellar Dust with Gaussian Processes

Andrew C. Miller
am5171@columbia.edu*

Lauren Anderson
anders.astro@gmail.com

Boris Leistedt
boris.leistedt@gmail.com

John P. Cunningham
jpc2181@columbia.edu

David W. Hogg
david.hogg@nyu.edu

David M. Blei
david.blei@columbia.edu

February 15, 2022

Abstract

Interstellar dust corrupts nearly every stellar observation, and accounting for it is crucial to measuring physical properties of stars. We model the dust distribution as a spatially varying latent field with a Gaussian process (GP) and develop a likelihood model and inference method that scales to millions of astronomical observations. Modeling interstellar dust is complicated by two factors. The first is *integrated observations*. The data come from a vantage point on Earth and each observation is an integral of the unobserved function along our line of sight, resulting in a complex likelihood and a more difficult inference problem than in classical GP inference. The second complication is *scale*; stellar catalogs have millions of observations. To address these challenges we develop ZIGGY, a scalable approach to GP inference with integrated observations based on stochastic variational inference. We study ZIGGY on synthetic data and the Ananke dataset, a high-fidelity mechanistic model of the Milky Way with millions of stars. ZIGGY reliably infers the spatial dust map with well-calibrated posterior uncertainties.

Keywords: Large-scale astronomical data, Gaussian processes, kernel methods, scalable Bayesian inference, variational methods, machine learning

1 Introduction

The Milky Way galaxy is primarily comprised of dark matter, stars, and gas. Within the gas, in its densest and coldest regions, dust particles form. The stars of the Milky Way are embedded in this field of dust.

Back on Earth, astronomers try to map the stars, measuring the location, apparent brightness, and color of each. But the dust between Earth and a star obscures the light, corrupting the astronomers' observation. Relative to the star's true brightness and color, the dust *dims* the brightness and *reddens* the color. This corruption is called *extinction*, and it complicates inferences about a star's true distance and other true properties. Stellar extinction has hindered many studies of stars in the Milky Way disk, which is where most dust lies, and therefore the largest extinctions (Mathis, 1990).

*Work done while at the Data Science Institute at Columbia University.

To cope with these corruptions, astronomers need a map of interstellar dust, an estimate of the density of dust at each location in the Galaxy. An accurate dust map could be used to correct our astronomical measurements and sharpen our knowledge of the Galaxy’s stars. Moreover, a dust map may be of independent scientific interest—for example, it may reveal macroscopic properties of the shape of the Milky Way, such as spiral arms.¹

But constructing such a map is difficult. We are embedded in our own dust field, and so we cannot directly observe it. Rather, we can only observe a noisy *integral* of the field along the line of sight between Earth and a star — the starlight extinction. (Here, the line of sight is the straight line through space between the star and the earth.) Thus the inference problem is to calculate a single, coherent spatial field of dust that can explain the observed extinction of millions of spatially distributed stars. In this paper, we use a large data set of astronomical measurements to infer a three-dimensional map of interstellar dust.

The data comes from standard practice in astronomy, which is to estimate the extinction of an individual star from its observed color and brightness using a physical model of star formation and evolution.² This procedure results in an estimate of the extinction and an approximate variance of the estimate about the true extinction value. However, this estimate is derived from a single star’s color and brightness—it ignores information about the spatial structure of the Milky Way and the fact that all stars are observed through the same three-dimensional density of dust.

The dust map is a spatial distribution of dust—an unobserved spatial function—that can help refine these noisy measurements. Each measurement is modeled conditional on the function and the three-dimensional location of the star.³ Such a model shrinks estimates toward their true values and reduces uncertainty about them. More formally, the unknown dust map is a function $\rho : \mathbb{R}^D \mapsto \mathbb{R}$ from a three-dimensional location in the universe x to the density of dust at that location. Our goal is to estimate this function from data.

We take a Bayesian nonparametric approach. We place a Gaussian process (GP) prior on the dust map and posit a likelihood function for how astronomical observations arise from it. We develop a scalable approximate posterior inference algorithm to estimate the posterior dust map from large-scale astronomical data. In addition to the scale of the data, the main challenge is the likelihood function. Typical spatial analysis involves data that are noisy evaluations of an unobserved function, and the likelihood is simple. Astronomical data, however, comes from a limited vantage point—we only observe the latent dust map as an *integrated process* along a line of site to a star, and this integral is baked into the likelihood of the observation.

More formally, let e_n be the true extinction of starlight for star n at location x_n , let a_n be the noisily measured extinction with uncertainty σ_n . Given the unknown dust map, we model the noisy measurement as a Gaussian whose mean is an integral from Earth to x_n (Rezaei Kh. et al., 2017). With covariance function $k_\theta(\cdot, \cdot)$, the full model is

$$\rho(\cdot) \sim GP(0, k_\theta(\cdot, \cdot)) \tag{1}$$

¹Though hints of spiral structures have been inferred from other observations (Georgelin and Georgelin, 1976; Chen et al., 2019), whether the Milky Way galaxy is a grand design spiral or if the spiral structures are more flocculent remains an open question. An accurate dust map will shed light on the recent dynamical history of the Milky Way.

²The observed color and brightness are directly derived from telescope images (e.g. photometry). Extinction measurements are backed out from a theoretical distribution of dust-free star colors and luminosities, where luminosity is the intrinsic brightness of a star. This distribution can be based on isochrones or empirically derived from a region of the sky known to have no dust (e.g. the Milky Way halo). The extinction corresponds to how far the observed color and brightness are from the set of theoretically plausible colors and luminosities. The extinction uncertainty incorporates both noise in the photometric measurement and prior uncertainty over the range of plausible colors and luminosities.

³The spatial locations of stars can be derived from parallax measurements. In this work we consider them fixed, but in future work will additionally consider their uncertainty.

$$a_n \sim \mathcal{N}(e_n, \sigma_n^2), \quad \text{where } e_n \triangleq \int_{x \in R_n} \rho(x) dx. \quad (2)$$

Here R_n is the set of points (i.e. the ray) from Earth to x_n ; the extinction e_n is in an integral of the latent dust map $\rho(\cdot)$, and it is through this integral that the map enters the likelihood. Figure 1 graphically depicts the distinction between pointwise and *integrated* observations.

The data are N locations, extinctions, and measurement errors, denoted $\mathcal{D} = \{a_n, x_n, \sigma_n^2\}_{n=1}^N$. Conditional on the data, we want to calculate the posterior dust map $\pi(\rho \mid \mathcal{D})$. This posterior can estimate different properties of the latent dust, e.g., the density of dust $\rho(\cdot)$ at a new location, the integral of dust $\rho(\cdot)$ over new sets, and posterior uncertainty about these values. Such inferences can aid many stellar studies.

But the posterior is difficult to compute, complicated by both the integrated likelihood and the large scale of the data. (Modern catalogs of astronomical data contain observations of millions of stars (Brown et al., 2018; Aguado et al., 2019).) In theory the scale is helpful—each star provides information about the unobserved dust map. But scaling a Gaussian process to millions of observations is a significant computational challenge.

We overcome these challenges with a scalable algorithm for Gaussian process inference with integrated observations, which we call ZIGGY.⁴ In particular, ZIGGY is a stochastic variational inference algorithm, one that uses stochastic optimization, inducing points, and variational inference to approximate the posterior. It handles general covariance functions and scales to millions of data points. We study ZIGGY on both synthetic data and the Ananke data, which comes from a high-fidelity mechanistic model of the Milky Way. We find that ZIGGY accurately reconstructs the dust map and accuracy continues to improve as the number of observations grows above a million.

In our applied setting, the integrated observations introduce technical challenges. ZIGGY builds upon an existing scalable Bayesian inference framework (Hoffman et al., 2013; Hensman et al., 2013), and introduces additional approximations and computational techniques to address the challenges created by integrated observations.

The paper is organized as follows. Section 2 describes related work for estimating interstellar dust. Section 3.1 formally sets up the problem and describes exact inference in GP models with integrated observations. Section 4 develops a stochastic variational inference algorithm that scales to millions of stellar observations. Appendix F studies ZIGGY on a synthetic two-dimensional example, comparing various settings of the algorithm that trade computation for accuracy and flexibility. Section 5 studies ZIGGY with the Ananke data set, showing that it recovers a well-calibrated three-dimensional dust map that accurately predicts extinctions and global dust structure. Section 6 concludes the paper and discusses directions for future research.

2 Related research

This work builds on a foundation of research in both astronomy and statistics.

Estimating the latent dust map. The seminal work of Schlegel et al. (1998) estimates the two-dimensional map of dust across the full sky using dust emission (rather than dust absorption, which we use here). Emission is a more direct estimate of the dust, but doesn’t allow for direct inferences of 3D structure. Stars within the Milky Way, however, are embedded in the three-dimensional dust field. Estimating per-star extinctions requires characterizing the dust field as a function of distance, motivating the construction of three-dimensional dust maps.

More recent approaches use hierarchical spatial models of noisy integrated observations to reconstruct three-dimensional maps. These approaches, however, rely on *discretizing space* and

⁴ZIGGY is named for Ziggy Stardust, David Bowie’s alter ego.

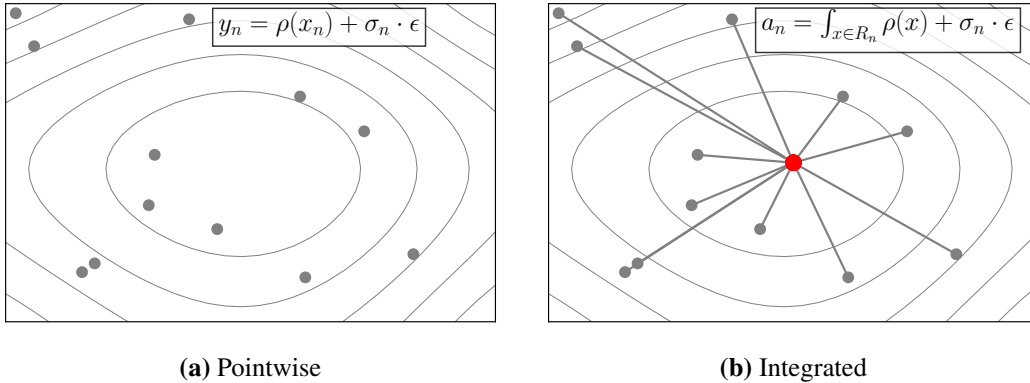


Figure 1: Reconstructing an unobserved function from pointwise (left) and integrated (right) observations. The latent function governs noisy pointwise observations, y_n , and integrated observations, a_n . The task is to reconstruct the unobserved function $\rho(x)$, depicted by the grey contours, everywhere in the domain. Our perspective is limited to the origin (red dot); our observations of this process are integrated along a compact set (i.e. a ray).

modeling integrated observations as finite sums. Various discretization strategies have been proposed, each with different computational demands.

One approach models discretized lines of sight to every star (Rezaei Kh. et al., 2017), but this approach can only accommodate a few thousand stellar observations. Another approach uses a fine mesh of cubic voxels to describe the dust distribution. This introduces a different computational trade off — larger voxels introduce unrealistic spatial artifacts (Green et al., 2018, 2019), while smaller voxels significantly increase the computational burden (Leike and Enßlin, 2019). Moreover, the theoretical length scale of the dust distribution is small; discretizing three-dimensional space with fine enough resolution to capture this small length scale will have to rely on additional approximations to scale to the entire volume of the Milky Way. The approach we develop here avoids discretization, works directly with continuous space, and scales to millions of observations.

Spatial statistics and Gaussian processes. The field of spatial statistics has developed many tools to estimate unobserved functions from noisy measurements (Cressie, 1992). One ubiquitous and fundamental method is Gaussian process regression or *kriging*, which interpolates or smooths a latent function given noisy observation at nearby locations (Krige, 1951; Matheron, 1963, 1973; Cressie, 1990; Rasmussen and Williams, 2006). A GP defines a probability distribution over the unobserved function that encodes prior assumptions about some properties — continuity, smoothness, and amplitude — while remaining flexible. GPs admit analytically tractable inference routines in typical settings, making them a useful prior for unobserved functions.

Scaling GPs to massive datasets is a more recent challenge. One approach is to approximate the GP with inducing point methods (Quiñonero-Candela and Rasmussen, 2005; Snelson and Ghahramani, 2006), where process values at specific places in the space, the inducing points, are learned from the data, and predictions are then produced using the inducing point process values. Inference using this approximation scales better than exact GP inference. Bolstering their use, recent theoretical work has characterized the error of inducing point GP approximations (Burt et al., 2019). However, inducing point methods still require analyzing the entire dataset simultaneously; this requirement limits their applicability to datasets where the number of observations is in the millions or billions.

Another thread of GP research in spatial statistics embeds them in more complicated models and scales them (Cressie, 1992; Banerjee et al., 2014). For example, nearest-neighbor GP’s are a scalable approximation for estimating the posterior of a latent spatial field (Datta et al., 2016). Similarly, the integrated nested Laplace approximations (INLA) framework is an approximate inference methodology that computes posterior marginal uncertainty in latent Gaussian models, including Gaussian process models with computationally tractable precision matrices (Rue et al., 2009). Several scalable Gaussian process approximations are reviewed in Heaton et al. (2019).

Gaussian processes have also been used within astronomy applications beyond building spatial maps of interstellar dust. Methods to scale one-dimensional GP regression to millions of observations have been developed and deployed with success (Ambikasaran et al., 2014; Foreman-Mackey et al., 2017).

Scalable Bayesian inference. We build on methods for scaling Bayesian inference to massive datasets. Variational methods (Jordan et al., 1999; Wainwright et al., 2008; Blei et al., 2017) are a computationally efficient alternative to Monte Carlo methods for posterior approximation. Variational inference treats approximate inference as an optimization problem, fitting a parameterized family to be close to the exact posterior. Stochastic optimization (Robbins and Monro, 1951) scales variational inference to large datasets, iteratively subsampling from the data to produce cheap, noisy gradients of the objective; this strategy is called stochastic variational inference (SVI) (Hoffman et al., 2013). Building off of SVI, stochastic variational Gaussian processes (SVGP) bring in inducing point methods to scale Gaussian processes to massive datasets (Hensman et al., 2013). We build on the SVGP framework here, adapting it to fit the GP model of astronomical data.

3 A Gaussian process model of starlight extinctions

The data are N stars, each one a tuple of its location x_n , a noisy measurement of the extinction a_n , and the variance of the observation σ_n^2 ; denote the data set $\mathcal{D} \triangleq \{x_n, a_n, \sigma_n^2\}_{n=1}^N$. Given the latent dust map $\rho(x)$, the likelihood of each observation a_n is defined in Equation 2, where the region of integration R_n is the ray that originates at the origin O (i.e. the Earth) and ends at the spatial location of the star, x_n ,

$$R_n = \{\alpha \cdot O + (1 - \alpha) \cdot x_n : \alpha \in [0, 1]\}. \quad (3)$$

To complete the model, Equation (1) places a Gaussian process prior on the dust map.

Given the data, the posterior distribution, $p(\rho | \mathcal{D})$, summarizes the evidence about the latent dust map. Via the relationship between $\rho(x_n)$ and e_n defined in Equation (2), we use this posterior over ρ to form estimates of the extinction for observed stars e_n , the extinction at new locations e_* , and the dust map itself at new locations $\rho(x_*)$. Specifically, we compute the posterior expectations

$$\hat{\rho}(x_*) \triangleq \mathbb{E}[\rho(x_*) | \mathcal{D}], \quad \hat{e}_n \triangleq \mathbb{E}[e_n | x_n, \mathcal{D}], \quad \hat{e}_* \triangleq \mathbb{E}[e_* | x_*, \mathcal{D}]. \quad (4)$$

The posterior variance, e.g., $\mathbb{V}[e_* | x_*, \mathcal{D}]$, describes the uncertainty of the estimates.

The posterior dust map $\rho(\cdot)$ synthesizes information from nearby sources to de-noise or shrink an individual extinction e_n , resulting in more accurate inferences with smaller estimator variance. Moreover it enables estimating the dust density at a new location x_* or to estimate the extinction along a path to the new point.

In the following sections we discuss how to calculate the posterior and how to approximate it with large data sets of stellar observations. Before that, however, we discuss the choice of a Gaussian process prior.

Why use a Gaussian process? First, Gaussian processes can flexibly model complex unobserved latent functions. The dust map $\rho(\cdot)$ is not easily described by a parametric functional form, but GPs can adapt highly complex, non-linear functions to describe data. Second, high-level properties of the unobserved dust map can be captured by the choice of the GP’s covariance function. In particular, we assume the dust map has specific structure—it is continuous and two nearby locations are more likely to have similar dust density values than two distant locations. GPs naturally capture such spatial coherence. Third, all stellar observations are derived from the same underlying dust map $\rho(x)$. Two noisy extinction measurements with nearby integration paths must be coherently described by a single estimate of $\rho(\cdot)$. The continuity, smoothness, and spatial coherence across observations give traction in forming an accurate statistical estimate of the unobserved dust map.

3.1 GP Inference with Integrated Observations

In a GP, any finite set of function evaluations are multivariate normal distributed with covariance defined by the covariance function, $\text{cov}(\rho(x_i), \rho(x_j)) = k_{\theta}(x_i, x_j)$. When observations are corrupted with Gaussian noise—the typical setting for GP models—the joint distribution between all observations and latent process quantities remains multivariate normal and the posterior at a new point $\rho(x^*)$ can be expressed as a few matrix operations (Rasmussen and Williams, 2006, Chapter 2). Inference in Gaussian process models with noisy *integrated observations*—defined in Equation 2—closely mirrors inference with the more typical, noisy pointwise observations.

Consider the model in Equations (1) and (2). We derive the posterior distribution by first characterizing the joint distribution over $\rho(x_*)$ and $\mathbf{a} = (a_1, \dots, a_N)$ (Rasmussen and Williams, 2006). Observe that linear operations of multivariate normal random variables remain multivariate normal in distribution. As noted in Rasmussen and Williams (2006, Section 9.8), because integration is a linear operation, the value of the integral of ρ over the domain \mathcal{X} will remain Gaussian. This is also true for any collection of definite integrals and the corresponding (Gaussian) noisy observations.

The joint distribution over \mathbf{a} and $\rho(x_*) \triangleq \rho_*$ remains multivariate normal. Given the mean and covariance of this joint distribution, we can compute the posterior distribution over ρ_* (or any set of ρ_* points) given observations \mathbf{a} , \mathbf{x} , and σ^2 . The joint distribution over \mathbf{a} and ρ_* mimics the standard Gaussian process setup

$$\begin{pmatrix} \mathbf{a} \\ \rho_* \end{pmatrix} \sim \mathcal{N} \left(\mathbf{0}, \begin{pmatrix} \mathbf{K}_e + \Sigma_a & \mathbf{K}_{e,*} \\ \mathbf{K}_{*,e} & \mathbf{K}_* \end{pmatrix} \right), \quad (5)$$

where the covariance matrix blocks are defined

$$(\mathbf{K}_e)_{ij} = \text{Cov}(e_i, e_j), \quad (\mathbf{K}_{*,e})_{*j} = \text{Cov}(\rho_*, e_j), \quad \mathbf{K}_* = \text{Cov}(\rho_*, \rho_*), \quad (6)$$

and the observation noise matrix $\Sigma_a \equiv \text{diag}(\sigma_1^2, \dots, \sigma_N^2)$. We note that because ρ_* is scalar, \mathbf{K}_* is a 1×1 matrix. Computing these covariance entries enables us to populate the joint covariance matrix and use standard multivariate normal conditioning for posterior inference. This conditioning mimics the equations for standard Gaussian process inference,

$$\rho(x_*) \sim \mathcal{N}(\mu_*, \Sigma_*) \quad (7)$$

$$\mu_* = \mathbf{K}_{*,e} (\mathbf{K}_e + \Sigma_a)^{-1} \mathbf{a} \quad (8)$$

$$\Sigma_* = \mathbf{K}_* - \mathbf{K}_{*,e} (\mathbf{K}_e + \Sigma_a)^{-1} \mathbf{K}_{e,*}. \quad (9)$$

To compute this posterior, we need to compute the covariances in Equation 6.

The chosen covariance function directly specifies $\text{Cov}(\rho_*, \rho_*)$. The other terms, $\text{Cov}(e_i, e_j)$ and $\text{Cov}(\rho_*, e_j)$ are slightly more complex, and require integrating the covariance function in one or both of its arguments.

Claim 3.1 (Semi-integrated Covariance Function). *The covariance between a process value $\rho_i \triangleq \rho(x_i)$ and an integrated value $e_j \triangleq \int_{x \in R_j} \rho(x) dx$ takes the form*

$$\text{Cov}(\rho_i, e_j) = \int_{x \in R_j} k(x_i, x) dx = k^{(\text{semi})}(x_i, x_j). \quad (10)$$

For consistency, we will write the integrated argument second.

The proof is in Appendix B.

Claim 3.2 (Doubly-integrated Covariance Function). *The covariance between two integrated process values e_i and e_j takes the form*

$$\text{Cov}(e_i, e_j) = \int_{(x, x') \in R_i \times R_j} k(x, x') dx dx' = k^{(\text{double})}(x_i, x_j). \quad (11)$$

The proof for the doubly-integrated kernel is similar to the semi-integrated case.

To summarize, if we can compute these two types of covariance values then we can plug the result into the distribution in Equation 5. As for standard GP inference, we can then manipulate the joint distribution using Gaussian conditioning to compute the posterior distribution over the value of the unobserved function $\rho(x_*)$ or functionals over test locations, for example integrated values e_* . Algorithm 1 summarizes GP inference using integrated measurements.

3.2 Choice of covariance function

Assumptions about the dust map $\rho(\cdot)$ can be encoded in the covariance function $k_\theta(\cdot, \cdot)$. We focus on kernels that are *stationary* and *isotropic*, which can be written $k_\theta(x, y) = \sigma^2 k\left(\frac{|x-y|}{\ell}\right)$ where $\theta \triangleq (\sigma^2, \ell)$. The parameter ℓ is the *length scale*, and the parameter σ^2 is the process marginal variance (Genton, 2001). The length scale controls how smooth the function is; the marginal variance influences the function’s amplitude. We will compare three families of kernel functions: squared exponential, Matérn, and a kernel from Gneiting (Gneiting, 2002). The squared exponential kernel — a commonly used covariance function for Gaussian process regression — admits an analytically tractable form for the semi-integrated kernel, but not the doubly integrated kernel. (See Appendix A.) Other kernels, such as the Matérn (Matérn, 1960) or the kernel presented in Gneiting (2002) do not readily admit a semi-integrated form, which complicates their use with integrated observations. Similarly, none of the mentioned kernels, including the squared exponential, admit a doubly-integrated form over two line segments. We develop a method to overcome this technical limitation in the following section. Furthermore, we use the analytic tractability of the semi-integrated kernel to validate this method on the squared exponential kernel.

Beyond the choice of covariance function family, the covariance function parameters (e.g. the length scale and process variance) ought to be tuned. Tuning GP covariance parameters can be complex — the process values ρ can strongly depend on parameters σ^2 and ℓ , making it difficult to explore their joint space. We discuss this phenomenon within the context of our scalable approximate inference algorithm in Section 4.

4 Scaling Integrated GP Inference

Gaussian process models scale poorly to large datasets (Quiñonero-Candela and Rasmussen, 2005; Titsias, 2009). Computing the posterior distribution of the latent function, the posterior predictive distribution of new observations, or the marginal likelihood of observed data (e.g. for model comparison) all require computing the inverse or the determinant of a $N \times N$ matrix — a $O(N^3)$ operation. As N grows larger than a few thousand observations, this computation becomes intractable. To address this bottleneck, a common strategy is to approximate Gaussian process inference using $M \ll N$ inducing points, or spatial locations in the input space that are used to approximate the full Gaussian process. Inducing point approximations can be interpreted in multiple ways. One interpretation is that the inducing points are used to construct a rank M approximation to the $N \times N$ matrix that can be efficiently inverted (e.g., $O(N \cdot M^3)$) (Quiñonero-Candela and Rasmussen, 2005). Another interpretation (which we adopt below), is that the inducing points are used to define a family of variational distributions for approximating the posterior over ρ , and optimizing the variational objective avoids direct manipulation of the $N \times N$ matrix (Titsias, 2009; Hensman et al., 2013).

Integrated observations create an additional computational issue — the semi-integrated or doubly-integrated covariance value between any two values may be unavailable in closed form (except in some special cases) and may require high-precision numerical approximation. With the integrated observations considered here, we have an additional computational issue. Calculating the semi-integrated or doubly-integrated covariance value between any two values may be unavailable in closed form (except in some special cases) and may require high-precision numerical approximation. The exact GP inference algorithm in Algorithm 1 requires computing a $N \times N$ matrix of doubly-integrated covariance values, which will be computationally prohibitive when N is a modest size. Furthermore, when tuning covariance function parameters or comparing covariance functions, the $N \times N$ matrix of numerically integrated covariance function values will need to be recomputed many times.

Thus, to use the model to analyze millions of integrated stellar observations, we derive a scalable variational inference algorithm to perform approximate posterior inference. Variational inference approximates a posterior distribution by optimizing a parameterized family—the variational distribution—to be close to the exact posterior (Jordan et al., 1999; Wainwright et al., 2008; Blei et al., 2017). For the model here, our approach builds on the stochastic variational Gaussian process (SVGP) framework (Hensman et al., 2013). It uses stochastic optimization to approximate the posterior (Hoffman et al., 2013), operating on small mini-batches of observations.

Further, to accommodate the integrated observations, we construct a Monte Carlo estimate of the semi-integrated kernel that generalizes to covariance functions that do not admit a closed form semi-integrated version. Additionally, we use the rotational invariance of stationary and isotropic covariance functions to construct a fast approximation to the doubly integrated covariance kernel.

This section describes the SVGP framework and our approach to adapt the framework to incorporate integrated observations. Section 4.1 describes relevant details of the SVGP framework, including inducing points, the variational family, and forming efficient mini-batch estimates of the variational objective. Section 4.2 details our approach to do inference with integrated observations for a general class of semi-integrated kernels.

4.1 Stochastic Variational Gaussian Processes

SVGP casts inference in GP models as an optimization problem. Crucially, the SVGP optimization objective is constructed such that it can be written as a sum of N terms, each depending on only

one data point. Given this construction, the objective can be optimized using stochastic gradients computed with mini-batches of data. This makes inference more computationally and memory efficient.

Here, we discuss the SVGP objective with the standard observations — noisy versions of $\rho(x)$. We then adapt this approximate inference framework to integrated observations in Section 4.2. Our derivation of the variational objective is slightly different from Hensman et al. (2013)—we first define a structured approximating family and then directly derive the evidence lower bound objective.

For this section’s presentation of inducing points, variational inference, and stochastic variational Gaussian processes, consider the typical GP model for N observations with $\rho \sim GP(0, k_\theta(\cdot, \cdot))$, and standard (i.e., non-integrated) observations $y_n | \mathbf{x}_n \sim \mathcal{N}(\rho(\mathbf{x}_n), \sigma_n^2)$. We write the observation vector $\mathbf{y} = (y_1, \dots, y_N)$ and the corresponding latent process vector $\boldsymbol{\rho} = (\rho(\mathbf{x}_1), \dots, \rho(\mathbf{x}_N))$.

Inducing points. Inducing points are a common tool used to scale Gaussian process inference (Quiñonero-Candela and Rasmussen, 2005). An inducing point is simply a location in the input space, \bar{x} , which has a corresponding inducing point value $\rho(\bar{x})$. Inducing points are typically distributed about the input space — in our experiments we place them on a fixed 3-dimensional grid throughout space.

We augment the model above with M inducing points and their corresponding values

$$\bar{\mathbf{x}} \triangleq \bar{\mathbf{x}}_1, \dots, \bar{\mathbf{x}}_M \quad \text{inducing points} \quad (12)$$

$$\mathbf{u} \triangleq \rho(\bar{\mathbf{x}}_1), \dots, \rho(\bar{\mathbf{x}}_M) \quad \text{inducing point values} \quad (13)$$

where \mathbf{u} is the M -length vector of values of ρ evaluated at each of the M inducing points. Note that the introduction of $\bar{\mathbf{x}}$ and \mathbf{u} has not altered the original model.

The model above specifies two latent variables, $\boldsymbol{\rho}$ and \mathbf{u} , whose distributions we wish to infer given data \mathbf{y} . That is, we wish to characterize the posterior distribution $p(\boldsymbol{\rho}, \mathbf{u} | \mathbf{y}, \mathbf{x}, \bar{\mathbf{x}})$ in a computationally efficient way.⁵ SVGP uses inducing points and a specific variational approximation to avoid the manipulation of the $N \times N$ observation covariance matrix.

Variational inference. Variational inference (VI) is an optimization-based approach to approximate posterior inference (Jordan et al., 1999; Wainwright et al., 2008; Blei et al., 2017). VI methods posit a *variational family* of distributions, $q \in Q$, and use optimization techniques to find the optimal approximate distribution from the set Q . Here, each element of Q is a distribution over the latent quantities — $q(\boldsymbol{\rho}, \mathbf{u})$.

The variational inference framework defines an objective to be optimized — the most common VI objective is the *evidence lower bound* (ELBO)

$$\mathcal{L}(q) = \mathbb{E}_{q(\boldsymbol{\rho}, \mathbf{u})} [\ln p(\boldsymbol{\rho}, \mathbf{u}, \mathbf{y} | \mathbf{x}, \bar{\mathbf{x}}) - \ln q(\boldsymbol{\rho}, \mathbf{u})] \leq \ln p(\mathbf{y} | \mathbf{x}, \bar{\mathbf{x}}). \quad (14)$$

Maximizing the ELBO minimizes the KL divergence between $q(\boldsymbol{\rho}, \mathbf{u})$ and the true posterior $p(\boldsymbol{\rho}, \mathbf{u} | \mathbf{y}, \mathbf{x}, \bar{\mathbf{x}})$.

Stochastic variational Gaussian processes The stochastic variational GP framework (SVGP) (Hensman et al., 2013) uses a particular form for the variational family. Given the set of inducing points $\bar{\mathbf{x}}$, the SVGP variational approximation is

$$q(\boldsymbol{\rho}, \mathbf{u}) = p(\boldsymbol{\rho} | \mathbf{u}) q_\lambda(\mathbf{u}), \quad q_\lambda(\mathbf{u}) \triangleq \mathcal{N}(\mathbf{u} | \mathbf{m}, \mathbf{S}), \quad \text{and } \boldsymbol{\lambda} \triangleq (\mathbf{m}, \mathbf{S}), \quad (15)$$

⁵Note that we are considering a model where the likelihood and prior are both Gaussian distributions — a conjugate pair — which implies that the posterior distribution will also be Gaussian. Indeed it will be, but manipulating Gaussian will scale cubically in N . The SVGP approach is constructed to scale linearly in N .

where $p(\boldsymbol{\rho} | \mathbf{u})$ is specified by the Gaussian process prior and recall that \mathbf{u} and $\boldsymbol{\rho}$ are jointly multivariate normal. The variational parameters $\boldsymbol{\lambda}$ are fit by optimizing the ELBO defined in Equation 14.

The SVGP approximation defined in Equation 15 is chosen because it has a very specific property — when plugged into Equation 14, the objective decomposes into the sum of N separate terms. This allows us to create unbiased *mini-batched* estimators of the objective (and its gradients), enabling efficient inference. We can see through a straightforward algebraic manipulation (we suppress ρ and \mathbf{u} 's dependence on \mathbf{x} and $\bar{\mathbf{x}}$ to remove clutter)

$$\mathcal{L}(\boldsymbol{\lambda}) = \mathbb{E}_{q(\boldsymbol{\rho}, \mathbf{u})} [\ln p(\boldsymbol{\rho}, \mathbf{u}, \mathbf{y}) - \ln q_{\boldsymbol{\lambda}}(\boldsymbol{\rho}, \mathbf{u})] \quad (16)$$

$$= \mathbb{E}_{q_{\boldsymbol{\lambda}}(\mathbf{u})p(\boldsymbol{\rho} | \mathbf{u})} [\ln p(\mathbf{y} | \boldsymbol{\rho}) + \overline{\ln p(\boldsymbol{\rho} | \mathbf{u})} + \ln p(\mathbf{u}) - \ln q_{\boldsymbol{\lambda}}(\mathbf{u}) - \overline{\ln p(\boldsymbol{\rho} | \mathbf{u})}] \quad (17)$$

$$= \underbrace{\mathbb{E}_{q_{\boldsymbol{\lambda}}(\mathbf{u})p(\boldsymbol{\rho} | \mathbf{u})} [\ln p(\mathbf{y} | \boldsymbol{\rho})]}_{(i)} - KL(q_{\boldsymbol{\lambda}}(\mathbf{u}) || p(\mathbf{u})) , \quad (18)$$

and we can write the term (i) as a sum over the N observations

$$(i) \triangleq \mathbb{E}_{q_{\boldsymbol{\lambda}}(\mathbf{u})} [\mathbb{E}_{p(\boldsymbol{\rho} | \mathbf{u})} [\ln p(\mathbf{y} | \boldsymbol{\rho})]] \quad (19)$$

$$= \mathbb{E}_{q_{\boldsymbol{\lambda}}(\mathbf{u})} \left[\mathbb{E}_{p(\boldsymbol{\rho} | \mathbf{u})} \left[\sum_{n=1}^N \ln p(y_n | \rho_n) \right] \right] \quad (20)$$

$$= \sum_{n=1}^N \underbrace{\mathbb{E}_{q_{\boldsymbol{\lambda}}(\mathbf{u})} [\mathbb{E}_{p(\boldsymbol{\rho} | \mathbf{u})} [\ln p(y_n | \rho_n)]]}_{\triangleq \mathcal{L}_n} . \quad (21)$$

When the likelihood $p(y_n | \rho_n)$ is Gaussian, the expectation in each of the \mathcal{L}_n terms can be computed analytically. Notice the cancellation in Equation 17 eliminates the term that involves all N data points and a $N \times N$ matrix inversion, $\ln p(\boldsymbol{\rho} | \mathbf{u})$ (Titsias, 2009).

To complete the derivation, we write a mini-batched estimator of the ELBO. Given a set of randomly selected observations B ,

$$\hat{\mathcal{L}}(\boldsymbol{\lambda}) = \frac{N}{|B|} \sum_{b \in B} \mathcal{L}_b - KL(q_{\boldsymbol{\lambda}}(\mathbf{u}) || p(\mathbf{u})) , \quad (22)$$

which is an unbiased estimator of the full objective, and only touches $|B| \ll N$ observations. We can use gradients of this estimator to optimize the lower bound with respect to variational parameters $\boldsymbol{\lambda} = (\mathbf{m}, \mathbf{S})$. With M inducing points, a mini-batched estimator can be computed in $O(|B| \cdot M^3)$ time.

When predicting, note that we only condition on the inducing point values \mathbf{u} , relying only on the prior covariance between \mathbf{u} and ρ_* . The structure of this variational approximation forces the inducing point values \mathbf{u} to represent all of the information learned from the data. While this approximation is no longer “nonparametric” in the traditional sense, it has been shown that inducing point methods can provide good approximations to exact GP inference provided enough inducing points are used (Burt et al., 2019). Empirically, we find that we can adequately tune covariance parameters and predict on held-out data using a modest number of inducing points (on the order of $M = 6,000$).

Natural gradients Given the objective in Equation 18, we are now tasked with finding the optimal parameters $\boldsymbol{\lambda}$. We use stochastic optimization with mini-batches (Hoffman et al., 2013) along with natural gradients (Amari, 1998), which are effective for variational inference of Gaussian processes (Hensman et al., 2013).

For exponential family distributions (e.g. the multivariate normal), the natural gradient can be computed by taking the standard gradient with respect to the mean parameters (Hoffman et al., 2013). Following Hensman et al. (2013), the natural gradient for variational parameters $\lambda = \mathbf{m}_\lambda, \mathbf{S}_\lambda$ is straightforward to express using the natural parameterization of the multivariate normal q_λ . See Appendix C for more details.

Whitened parameterization. Draws of $\mathbf{u} \sim p(\mathbf{u} | \bar{\mathbf{x}}, \boldsymbol{\theta})$ are highly dependent on $\boldsymbol{\theta}$. Consider a draw \mathbf{u} conditioned on a fixed length scale parameter of ℓ . This same draw will be highly improbable under the prior with a different length scale parameter, e.g. 2ℓ . The variational approximation λ targets the posterior distribution $p(\mathbf{u} | \mathbf{y}, \boldsymbol{\theta})$, which is highly dependent on the structured Gaussian process prior. This dependence frustrates the joint inference of λ and $\boldsymbol{\theta}$ — small changes in $\boldsymbol{\theta}$ can make the approximate distribution over \mathbf{u} suboptimal. This dependence forces gradient methods to take small steps, which leads to extremely slow joint inference.

An effective strategy for coping with this dependence is to do posterior inference in an alternative parameterization of the same model that decouples variables \mathbf{u} and $\boldsymbol{\theta}$. For structured latent Gaussian models (e.g. Gaussian processes) this alternative model uses the *whitened* prior (Murray and Adams, 2010) or *non-centered* parameterization (Bernardo et al., 2003). For the dust map model, we whiten the prior by altering the target of posterior inference — instead of approximating the posterior over inducing point values $p(\mathbf{u} | \mathbf{y}, \boldsymbol{\theta})$, we target the posterior over inducing point *noise* values $p(\mathbf{z} | \mathbf{y}, \boldsymbol{\theta})$, where the relationship between \mathbf{z} and \mathbf{u} is constructed to produce an equivalent model. For notational clarity, we define $\mathbf{K} \triangleq \mathbf{K}_{\mathbf{u},\mathbf{u}}^{(\boldsymbol{\theta})}$ for a fixed value of $\boldsymbol{\theta}$ and \mathbf{L} such that $\mathbf{K} = \mathbf{L}\mathbf{L}^\top$ is a general matrix square root. The whitened model can be written

$$\mathbf{z} \sim \mathcal{N}(0, I_M), \quad \mathbf{u} \triangleq \mathbf{L}\mathbf{z} \sim \mathcal{N}(0, \mathbf{K}). \quad (23)$$

We now target the posterior distribution $p(\mathbf{z} | \mathbf{y}, \boldsymbol{\theta})$ by fitting an approximation $q_\lambda(\mathbf{z}) = \mathcal{N}(\mathbf{z} | \tilde{\mathbf{m}}, \tilde{\mathbf{S}})$. The linear relationship between \mathbf{z} and \mathbf{u} implies that $\mathbf{m} = \mathbf{L}\tilde{\mathbf{m}}$ and $\mathbf{S} = \mathbf{L}\tilde{\mathbf{S}}\mathbf{L}^\top$. We describe additional details of this parameterization in Appendix D.

4.2 Adapting to integrated observations

The previous section detailed a scalable approximate inference algorithm for Gaussian processes in the typical noisy pointwise observation setting. Here, we adapt this framework to integrated observations. The challenge is now efficiently computing the appropriate semi- and doubly-integrated covariance values to be used within each mini-batch update.

The natural gradient described in Equation 39 consists of two types of covariance matrices — $\mathbf{K}_{\mathbf{u},\mathbf{u}}$ and $\mathbf{K}_{\mathbf{u},\rho}$. The former describes the prior covariance between inducing point values and remains exactly the same in the integrated observation setting. The latter describes the cross covariances between process locations and inducing point values — this cross covariance must be adjusted to reflect the covariance between the *integrated process* and the inducing point values. This is precisely what is defined by the semi-integrated covariance function. The entries of $\mathbf{K}_{\rho,\mathbf{u}}$ have to simply be switched to the semi-integrated covariance defined in Claim B.1

$$(\mathbf{K}_{\rho,\mathbf{u}})_{n,m} = \int_{x \in R_n} k(x_m, x) dx. \quad (24)$$

In addition to the semi-integrated cross covariances, ZIGGY will need to calculate doubly-integrated covariance terms. First, note that the gradient defined in Equation 39 does not require doubly integrated terms. This is convenient — the inducing point method does not require cross covariances between integrated observations, and these cross covariances also happen to be the

most expensive to approximate with numerical methods. However, computing the variational objective (Equation 18) and making predictions (Equation 78) do require the doubly-integrated diagonal terms, $\mathbf{K}_{n,n}$ for each observation.

Given the above dependence on integrated covariance terms, the full adaptation of the SVGP method to integrated observations runs into two technical hurdles. First, the semi-integrated covariance is not available in closed form beyond the simple squared exponential, which is considered too smooth (and thus of limited capacity) in many settings. This limitation will make it difficult to use custom covariance kernels constructed with astronomical theory (Leike and Enßlin, 2019). Further, it will make it difficult to compare different models and choose the best predictor among them. Second, even when the semi-integrated covariance kernel is available in closed form, the doubly-integrated covariance is not. The SVGP (and any inducing point) algorithm only relies on *the diagonal* of the covariance kernel, so we only need to approximate this diagonal, scalar-valued function. We show that this scalar-valued function can be easily approximated using a small grid of interpolated values, where the “true” values are approximated using numerical integration.

We introduce two computationally efficient approximations to these operations on the covariance function to overcome these technical issues: (i) Monte Carlo estimates for semi-integrated covariance functions and (ii) linear interpolation for the doubly-integrated diagonal covariance function.

Monte Carlo estimators for semi-integrated kernels The natural gradient updates in Equation 39 require computing the covariance between observations and inducing point values, $\mathbf{K}_{\rho,u}$. For integrated observations, the covariance between observations and inducing points is given by the semi-integrated kernel in Equation 24. For kernels with a closed form semi-integrated kernel (e.g. the squared exponential), we can simply substitute $k^{(semi)}(\bar{x}_m, x_n)$ for $k(\bar{x}_m, x_n)$ in the loss and gradients and proceed within the typical SVGP framework.

For kernels without a closed form semi-integrated kernel, we run into a computational issue — how do we compute the appropriate cross covariance values? One approach is to use numerical integration — the semi-integrated covariance is a one-dimensional integral that can be approximated with quadrature techniques. However, each batch requires computing $M \times |B|$ semi-integrated covariance values — this can be computationally expensive, which would force us to use small batches, and this leads to slower learning.

Stochastic natural gradient updates are already an estimate of the true gradient — how *good* does this estimate have to be to effectively find the optimal solution? Numeric integration approximations to $k^{(semi)}(\cdot, \cdot)$ are precise to nearly machine precision, but are computationally expensive. Analogously we can ask, how *good* do the semi-integrated covariance approximations have to be to effectively find the optimal solution?

Pursuing this idea, we propose using a Monte Carlo approximation to the semi-integrated covariance values — we sample uniformly along the integral path and average the original covariance values. More formally, we introduce a uniform random variable ν_{R_n} that takes values along the ray R_n from the origin to x_n . We can now write the semi-integrated covariance as

$$k^{(semi)}(x_m, x_n) = \int_{x \in R_n} k(x_m, x) dx = |R_n| \int_{\nu \in R_n} \underbrace{\frac{1}{|R_n|}}_{=p(\nu)} k(x_m, x) dx = |R_n| \mathbb{E}_{\nu} [k(x_m, \nu)] .$$

This form admits a simple Monte Carlo estimator

$$\nu^{(1)}, \dots, \nu^{(L)} \sim \text{Unif}(R_n), \quad \hat{k}^{(semi)}(x_m, x_n) = \frac{|R_n|}{L} \sum_{\ell} k(x_m, \nu^{(\ell)}) . \quad (25)$$

It is straightforward to show that Equation 25 is an unbiased and consistent estimator for the true semi-integrated covariance value evaluated at x_m and x_n . While plugging this directly into the gradient formula results in a biased estimator for the natural gradient, we find that with a modest number of samples we can closely match the optimization performance of the true natural gradient estimator. We investigate the relationship between samples L and the resulting optimization in Appendix Figure 9. Appendix E.1 contains additional details and experimental results validating this approach.

Although conceptually similar, note that this Monte Carlo estimate of the semi-integrated covariance is not equivalent to discretizing along each line of site as in (Rezaei Kh. et al., 2017). The estimator can use a small number of samples along the ray and still be useful within stochastic gradient optimization.

Integrated Observation Variance. The SVGP algorithm requires an additional covariance calculation — the marginal variance of an integrated observation at point x_n , $k^{(\text{doubly})}(x_n, x_n)$. Note that we do not need to compute the non-diagonal terms of the doubly integrated kernel, a consequence of the separability of Equation 21. Similar to the semi-integrated kernel function, the doubly integrated function can be approximated with numerical methods — a double quadrature routine for each observation. But, similar to the semi-integrated case, this double quadrature call becomes a computational bottleneck within each batch. Furthermore, computing the gradient of the ELBO with respect to the covariance parameters with autodifferentiation tools would require differentiating through a double quadrature call — prohibitive in our setting.

We solve this problem by observing that a rotationally invariant (and stationary) kernel admits a doubly-integrated version that is a function only of the distances to each of the two integral endpoints. That is, $k^{(\text{doubly})}(x_i, x_j)$ can be written as a function $f(|x_i|, |x_j|)$ for a fixed setting of covariance function parameters. Further, we can write the diagonal of the doubly-integrated kernel as a function of only the distance to the single point, $k^{(\text{doubly})}(x_n, x_n) = f(|x_n|)$.

Given that this is a one-dimensional function shared by all N of our observations, we approximate the doubly-integrated kernel diagonal with linear interpolation. The interpolation scheme allows us to cheaply compute a highly accurate approximation to the doubly-integrated diagonal. It also enables us to easily backpropagate gradients to the kernel function parameters, which enables efficient tuning during the variational inference optimization routine. Appendix E.2 describes the interpolation scheme for $k^{(\text{doubly})}(x_n, x_n)$ in further detail.

4.3 Method summary and remarks

To summarize, ZIGGY scales Gaussian process inference with integrated observations by fusing several strategies: (i) the explicit representation of the inducing point posterior within the SVGP framework; (ii) a whitened parameterization to decouple λ and θ in the variational objective; (iii) on-the-fly Monte Carlo estimates of the semi-integrated covariance function; (iv) and fast kernel interpolation of the doubly integrated diagonal covariance function that leverages the stationary and isotropic properties of the covariance functions considered.

Algorithm 2 describes the main loop for updating based on stochastic gradients of the variational parameters and the covariance function parameters θ . Maximizing the variational lower bound (Equation (18)) with respect to prior parameters θ is a similar strategy to empirical Bayes (Efron et al., 2008; Efron, 2019), a method used to reduce the average error of posterior estimates.

We find that the inducing point approach dovetails nicely with integrated observations—most evaluations of the covariance function are between inducing points and observations. This only requires computing the (easier) semi-integrated covariance function. Further the doubly-integrated covariance values between any two distinct observations never needs to be computed. Rather, only

the *diagonal* of this covariance function needs to be computed, but this conveniently reduces to a one-dimensional function that can be efficiently approximated. ZIGGY circumvents computing the (prohibitive) $N \times N$ doubly-integrated covariance.

We note that the SVGP framework for scaling Gaussian process is one approach to build upon for our application — other frameworks for scaling kernel methods could have been employed. One example is random (or carefully selected) features for approximating the kernel function (Rahimi and Recht, 2008; Yang et al., 2012; Le et al., 2013). While these approximate kernel methods could yield superior performance, one reason we reach for the SVGP framework is extensibility. The variational inference framework can incorporate more complex probabilistic graphical model structure. For this application, additional types of observations can be incorporated into a more sophisticated likelihood model to help identify the spatial dust distribution and incorporate additional sources of uncertainty.

5 Validation with a Domain Simulation

We developed ZIGGY with the goal of generating a three-dimensional dust map of the Milky Way using 2 billion stars in the Gaia dataset (Brown et al., 2018). As a step towards that goal—and to test ZIGGY in an applied environment—we infer the dust distribution of a mechanistic and physically motivated domain simulation. The domain dataset is a synthetic Gaia survey of a high resolution Milky Way-like galaxy simulation.

The domain dust density $\rho(x)$ was generated in a Milky Way-like galaxy simulation, one of many in the Latte suite of simulations of Milky-Way-mass galaxies (Wetzel et al., 2016; Hopkins et al., 2018). It was run as part of the Feedback In Realistic Environments (FIRE) simulation project, which self-consistently models extinction and star formation in a cosmological context at high resolution.

In astronomy, most observations prefer a model in which our Universe is predominantly made of cold dark matter (Aghanim et al., 2018). On small scales, however, there are significant challenges to this model (Klypin et al., 1999), which this suite of simulations helps resolve (Wetzel et al., 2016). This Latte simulation overcomes the computational challenge of including gas, dust, and stars with high enough resolution to resolve these tensions. It includes more complex physics of “normal” matter, as apposed to just dark matter, including a high resolution disk of gas and dust. Because of the results from these simulations, which resolved these tensions, astronomers are more confident in a universal model of dark matter.

The simulation has enough resolution to resolve the formation of structures in the dense gas that forms dust and stars, creating a realistic environment for inference. The positions of the extinction observations, or the positions of stars within $\rho(\cdot)$, was generated by the Ananke framework. The Ananke framework generated a realistic, mock star catalog from the FIRE simulation, and kept intact important observational relationships between gas, extinction, and stellar populations (Sanderson et al., 2018). This catalogue was specifically designed to resemble a Data Release 2 Gaia astrometric survey (Brown et al., 2018), with a similar resolution of stellar density as Gaia. We integrated $\rho(x)$ along lines of sight to 1 million stars in the Ananke dataset within a $0.5\text{kpc} \times 0.5\text{kpc} \times 0.1\text{kpc}$ region of the synthetic sun. So, we generate a set of N noisy integrated observations

$$x_n \sim \text{Ananke}(\mathcal{X}) \quad \text{stellar locations} \quad (26)$$

$$e_n = \int_{x \in R_n} \rho(x) dx \quad \text{domain extinctions} \quad (27)$$

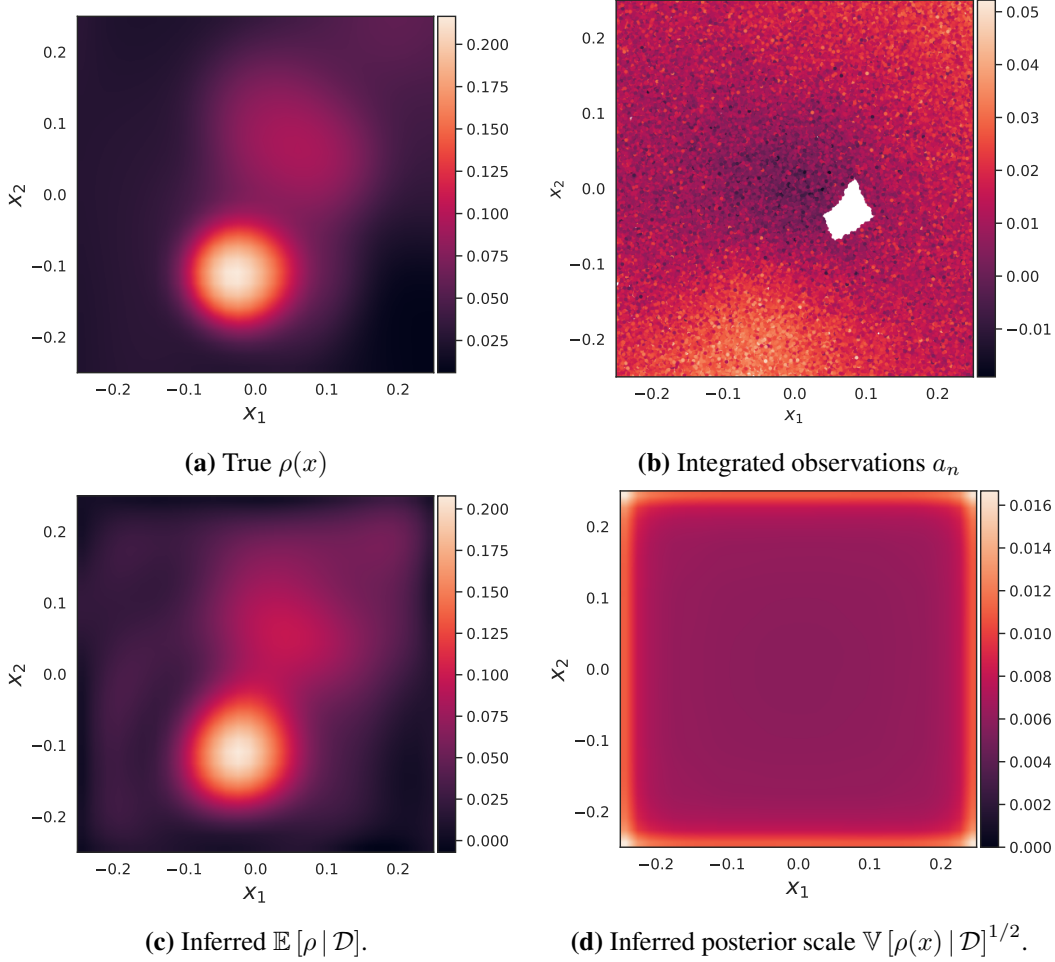


Figure 2: Integrated observation GPs can reveal spatial structure from a severely limited vantage point. This figure summarizes domain simulated data posterior inference using $N = 1,000,000$ examples in a three-dimensional space. Panel 2a depicts the true (unobserved) $\rho(x)$ that generates the data. Panel 2b depicts the observed data, noisy integrated measurements of ρ from the origin to stellar positions in the domain simulation. 2c depicts the inferred ρ given these observations using ZIGGY with a squared exponential kernel. 2d depicts the marginal posterior standard deviation at each location in \mathcal{X} -space. All Panels are a slice at $z = 0$

$$a_n \sim \mathcal{N}(e_n, \sigma_n^2) \quad \text{noisy integrated observation} \quad (28)$$

where the domain $\mathcal{X} = [(-0.25, 0.25), (-0.25, 0.25), (-0.05, 0.05)]$, the median extinction value is 0.01, and noise variance is chosen to be $\sigma_n = 0.005$. So our median signal-to-noise value is 3. The true extinctions, e_n , are computed to high precision using numerical quadrature, integrating from the origin to the Ananke stellar locations x_n . The integrated observations are depicted in Figure 2b. We estimate this domain specific dust density $\rho(\cdot)$ from noisy integrated observations using ZIGGY.

In Section 5.1, we compare posterior estimates of $\rho(\cdot)$ as a function of training data set size. This highlights the importance of scaling inference to more observations in order to obtain a more accurate statistical estimator. In Section 5.2, we compare posterior estimates of $\rho(\cdot)$ as a function of kernel choice, with a fixed data set size.

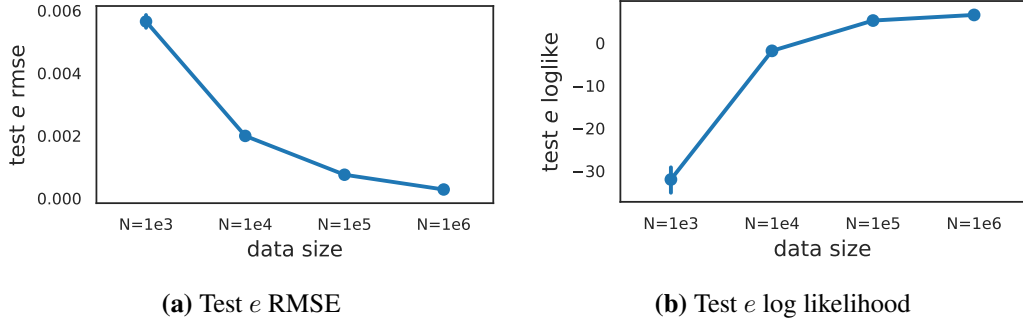


Figure 3: Scaling to massive N improves estimator performance. We compare predictive RMSE (left) and log likelihood (right) as a function of data set size N on a held out sample of test stars.

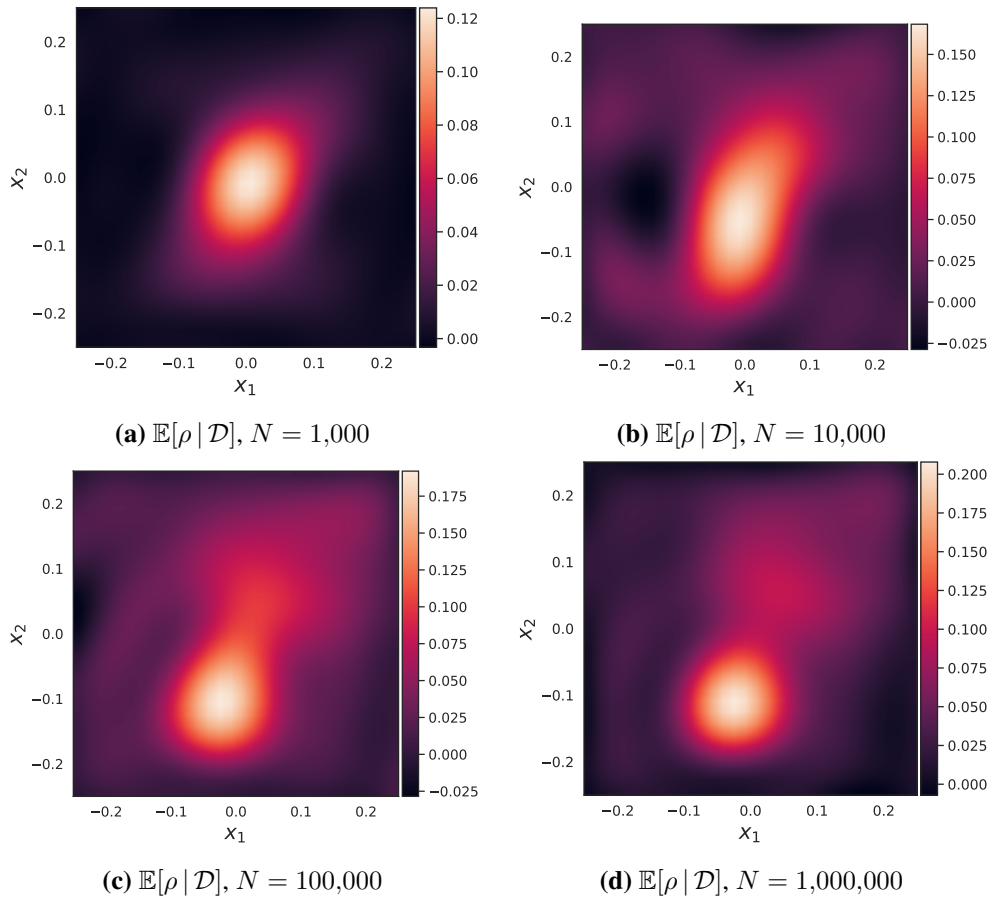


Figure 4: Slices of the posterior mean function at $z = 0$ for various dataset sizes. More data leads to more accurate predictions of $\rho(\cdot)$.

5.1 The quality of the estimate

We study the quality of the estimate of $\rho(x)$ as a function of data set size N . We fit the dust model to the Ananke dataset with data set sizes $N \in \{10^3, 10^4, 10^5, 10^6\}$ for $10^5, 10^4, 10^3, 100$ epochs, respectively. We trained each model using mini-batches of size $|B| = 2,000$, an initial step size of 0.01, reducing it every epoch by multiplying by a decay factor of 0.99. We measure model quality

by computing root mean squared error (RMSE) and log likelihood (LL) on a set of $N_{\text{test}} = 2,000$ held out extinction values. Each model uses $M = 16 \times 16 \times 4$ inducing points, evenly spaced in a grid in the input space.

Figure 2 summarizes the model’s fit using one million observations, the most we tried in this example. Figure 2c displays the posterior mean for $\rho(x)$ given the one million observations depicted in 2b. Figure 2d shows the posterior uncertainty (one standard deviation) about the estimated mean. We see that the million-observation model recovers the true latent function particularly well.

Figure 3 quantifies the improvement in the RMSE and log likelihood on a held out sample of test stars as a function of dataset size N . As the dataset size increases, both statistics drastically improve. Figure 4 visualizes a direct comparison of the posterior estimate of the latent function as we increase data set size N . We can clearly see that as we incorporate more data into the nonparametric model, the form of the true underlying function emerges. To accurately visualize and interpret large scale features of the latent dust distribution, we will want to incorporate as many stellar observations as possible. This is particularly true in the low signal to noise regime of extinction estimates.

5.2 Comparing kernels

Similar to the synthetic dataset, we compare multiple models by fitting the variational approximation and tuning the covariance function parameters for 5 different kernel choices.

In this domain setup, we ran each model for 100 epochs, saving the the model with the best ELBO value. We used mini-batches of size $|B| = 2,000$, and started the step size at 0.01, reducing it every epoch by multiplying by a decay factor of 0.99. For kernels that do not have a closed form semi-integrated version, we used $L = 50$ uniform grid Monte Carlo samples to estimate the integrated covariance.

We validate the inferences against a set of 2,000 held-out test extinctions e_* . We quantify the quality of the inferences with mean squared error, log likelihood, and the χ^2 -statistic on the test data. We also visually validate ZIGGY with a QQ-plot and coverage comparison, also on test data. We also visualize the behavior of ZIGGY as a function of distance to the origin — specifically, we visualize how accurate and well-calibrated test inferences are as synthetic observations are made farther away.

In Figure 5 we compare the mean squared error (MSE), the log likelihood, and the χ^2 statistic on the held out test data. We compare five different kernels – (i) Gneiting $\alpha = 1$ from [Rezaei Kh. et al. \(2018\)](#) (ii-iv) Matérn, $\nu \in \{1/2, 3/2, 5/2\}$, and (v) the squared exponential kernel. The results match our expectations. The true $\rho(\cdot)$ is quite smooth, and we see that the smoother kernels tend to have lower predictive error and higher log likelihood. All kernels have similarly calibrated χ^2 statistic, except for Matérn, $\nu = 3/2$, which under predicts it’s posterior variances. This can also be seen in Figure 6. The test statistic comparison has chosen a good match in the squared exponential kernel.

To test the calibration of posterior uncertainties, we inspect statistics of test-sample z -scores for e_* . We test that the statistics of predictive z -scores resemble a standard normal distribution using a QQ-plot. For a more detailed description fo the QQ-plot, please see Section F.2. To compare different models, we visualize QQ-plots for the different covariance functions in Figure 6. As an additional summary of calibration, we compare the fraction of predicted examples covered by $1/2, 1, 2$, and 3 posterior standard deviations, summarized in Table 1. We see that there is room for improvement in the posterior variances. The z -scores and empirical coverage show posterior variances that are well calibrated for the squared exponential and Matérn, $\nu = 5/2$ kernels, but are too large for the other kernels. The models for the less smooth kernels are compute bound,

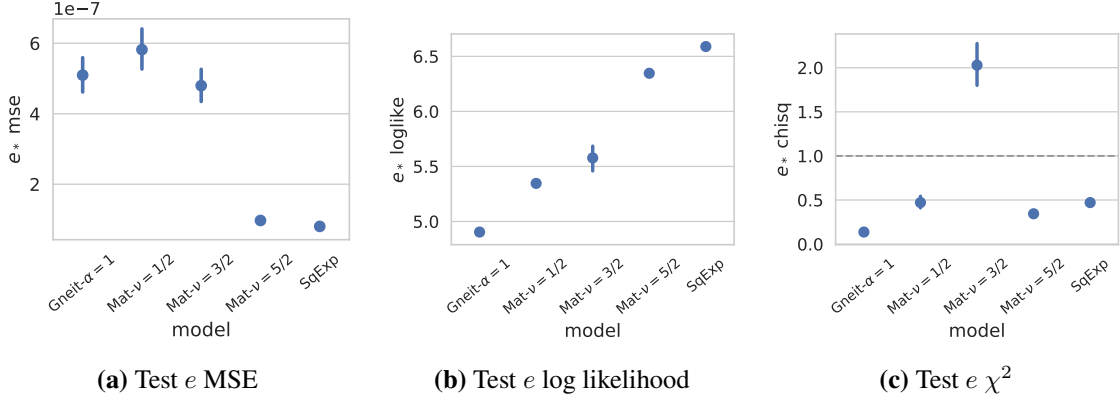


Figure 5: Predictive summaries across different models and inference schemes. The smoother models have better predictive summary statistics which is consistent with the underlying density field being very smooth.

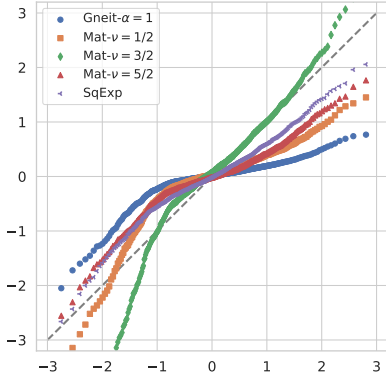


Figure 6: QQ-plot for predicted distributions on 2,000 held out integrated- ρ test points e_* . Theoretical normal quantiles are on the horizontal axis, and predictive z -scored quantiles are on the vertical axis. Posterior for extinctions e are moderately well calibrated, with the squared exponential kernel having the best calibration.

requiring thousands of inducing points to tile the domain. We ran the models for 100 epochs, which maxed out the memory and compute time. Miscalibration could be the result of misspecification of the model itself — e.g., mismatch between the covariance function k and the true underlying ρ , or the inflexibility of the variational approximation. To diagnose this shortcoming, methods that allow us to scale the expressivity of the variational approximation — e.g., larger M — would be necessary.

We also depict model fit statistics as a function of distance from the origin in Figure 7. Figure 7a visualizes the test extinction values. ZIGGY is able to accurately reconstruct the dust map. Figure 7b shows the posterior standard deviation by distance, which shows a noise reduction of about $10\times$ for most stars. In Figure 7c we see that the predictions have posterior variances that are slightly too high, causing z -scores that lie mostly within 2σ independent of distance, with only the most nearby stars extending to 3σ . Decent calibration, including at far distances, is encouraging, as the goal is to form good estimates of this density far away from the observer location.

6 Discussion

Mapping the three-dimensional distribution of dust in the Milky Way is fundamental to astronomy. Star dust obscures our observations of star light, and so an accurate dust map would help us more

	Gneit- $\alpha = 1$	Mat- $\nu = 1/2$	Mat- $\nu = 3/2$	Mat- $\nu = 5/2$	SqExp	$\mathcal{N}(0, 1)$
σ						
0.5	0.894	0.760	0.451	0.730	0.625	0.383
1.0	0.965	0.900	0.677	0.900	0.869	0.683
2.0	0.997	0.969	0.878	0.991	0.986	0.955
3.0	1.000	0.994	0.947	1.000	0.999	0.997

Table 1: Coverage fractions at various levels of z-score standard deviation σ for test extinctions e_* . Compared with theoretical coverage fractions, we see that our inferences generate predictions that are well calibrated for the smoothest kernels

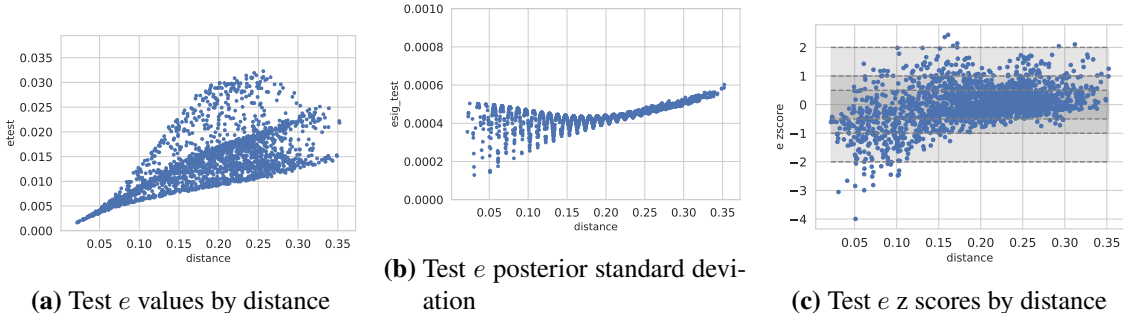


Figure 7: Posterior summaries as a function of distance to the origin (observation point). The noise variance for the extinction estimates is $\sigma_n = 0.005$, so Figure a demonstrates our low signal to noise regime, Figure b demonstrates our shrinkage by a factor of 10, and Figure c demonstrates our decent calibration in this very low signal to noise regime.

clearly observe the universe. Such a dust map would be a new lens into the dynamics of the Milky Way, providing a trace of the process by which it formed.

In this paper, we developed ZIGGY, a method to estimate the dust map from millions of astronomical observations. ZIGGY incorporates noisy information into a single, coherent spatial model. We developed technical innovations to accommodate integrated observations into the Gaussian process framework, and to scale such a model to millions of observations without spatial discretization. We validated these algorithmic innovations with numerical studies, and measured the performance of ZIGGY in both a synthetic setting and a realistic, high-fidelity dataset used in astronomical study. We showed that ZIGGY is able to incorporate millions of observations and recover accurate and well-calibrated estimates of both stellar extinctions and pointwise values of the three-dimensional dust map.

There are several avenues for future research and improvement. ZIGGY assumes that distances are known, when in reality they are noisy. In practical applications, we will only include stars with precise distance measurements, lowering the spatial density of observations, which may degrade estimates. We view ZIGGY as a step toward a probabilistic model of photometric measurements that jointly infers brightnesses, colors, distance, and spatial dust. Jointly modeling brightnesses, distances, and a spatial dust map using a Bayesian hierarchical model will allow us to leverage the coherence of Bayesian probabilistic modeling to form tighter estimates of all modeled quantities.

Additionally, a limitation of our treatment is the Gaussian error assumption. Non-Gaussian observation errors could degrade extinction estimates — e.g., forcing ρ to be more complex (i.e., with a smaller length scale) than it truly is. A flexible hierarchical Bayesian model could incorporate

a non-Gaussian likelihood that could be more robust to heavier tailed observation error.

A full map that spans the entirety of the Milky Way will require increasing the capacity of the approximation. To reconstruct both global and local features using an inducing point method, we need to ensure that small length scales (relative to the input domain) can be resolved. When inducing points are spatially distant from one another, the inducing point approximation will not have the capacity to represent sharp changes in $\rho(x)$ at small scales. This limitation can be overcome by including more, and closer, inducing points. However, introducing more inducing points butts up against the $O(M^3)$ computational limitations. In this work, we assume we are able to populate the space with enough inducing points; but the scaling concern is an important avenue of future work. Incorporating more inducing points will be crucial to resolving both global features and fine local features within the Milky Way.

The ultimate goal of this line of work is to produce an accurate catalog of the properties of stars, such as probabilistic brightnesses and distances, and the focus of scale is motivated by the size of modern photometric catalogs. PAN-STARRS 1 catalog includes 2.4 million detected stars (Flewelling, 2016), the fifteenth data release of the Sloan Digital Sky Survey includes photometry for over 260 million detected stars (Aguado et al., 2019), and the second GAIA data release has 1.3 billion stars with parallax measurements that can be used to estimate the interstellar dust distribution (Brown et al., 2018). As a final avenue of research, we will scale ZIGGY to incorporate billions of observations in a much larger spatial domain.

References

- Aghanim et al., N. (2018). Planck 2018 results. VI. Cosmological parameters. *arXiv e-prints*, page arXiv:1807.06209.
- Aguado, D. S., Ahumada, R., Almeida, A., Anderson, S. F., Andrews, B. H., Anguiano, B., Ortíz, E. A., Aragón-Salamanca, A., Argudo-Fernández, M., Aubert, M., et al. (2019). The fifteenth data release of the sloan digital sky surveys: first release of manga-derived quantities, data visualization tools, and stellar library. *The Astrophysical Journal Supplement Series*, 240(2):23.
- Amari, S.-I. (1982). Differential geometry of curved exponential families—curvatures and information loss. *The Annals of Statistics*, pages 357–385.
- Amari, S.-I. (1998). Natural gradient works efficiently in learning. *Neural computation*, 10(2):251–276.
- Ambikasaran, S., Foreman-Mackey, D., Greengard, L., Hogg, D. W., and O’Neil, M. (2014). Fast direct methods for Gaussian processes. *arXiv preprint arXiv:1403.6015*.
- Banerjee, S., Carlin, B. P., and Gelfand, A. E. (2014). *Hierarchical modeling and analysis for spatial data*. Chapman and Hall/CRC.
- Bernardo, J., Bayarri, M., Berger, J., Dawid, A., Heckerman, D., Smith, A., and West, M. (2003). Non-centered parameterisations for hierarchical models and data augmentation. In *Bayesian Statistics 7: Proceedings of the Seventh Valencia International Meeting*, volume 307. Oxford University Press, USA.
- Blei, D. M., Kucukelbir, A., and McAuliffe, J. D. (2017). Variational inference: A review for statisticians. *Journal of the American Statistical Association*, 112(518):859–877.

- Brown, A., Vallenari, A., Prusti, T., De Bruijne, J., Babusiaux, C., Bailer-Jones, C., Biermann, M., Evans, D. W., Eyer, L., Jansen, F., et al. (2018). Gaia data release 2-summary of the contents and survey properties. *Astronomy & astrophysics*, 616:A1.
- Burt, D. R., Rasmussen, C. E., and van der Wilk, M. (2019). Rates of Convergence for Sparse Variational Gaussian Process Regression. *arXiv preprint arXiv:1903.03571*.
- Chen, B.-Q., Huang, Y., Hou, L.-G., Tian, H., Li, G.-X., Yuan, H.-B., Wang, H.-F., Wang, C., Tian, Z.-J., and Liu, X.-W. (2019). The Galactic spiral structure as revealed by O- and early B-type stars. *Monthly Notices of the Royal Astronomical Society*, 487:1400–1409.
- Cressie, N. (1990). The origins of kriging. *Mathematical geology*, 22(3):239–252.
- Cressie, N. (1992). Statistics for spatial data. *Terra Nova*, 4(5):613–617.
- Datta, A., Banerjee, S., Finley, A. O., and Gelfand, A. E. (2016). Hierarchical nearest-neighbor Gaussian process models for large geostatistical datasets. *Journal of the American Statistical Association*, 111(514):800–812.
- Efron, B. (2019). Bayes, oracle bayes and empirical bayes. *Statistical science*, 34(2):177–201.
- Efron, B. et al. (2008). Microarrays, empirical bayes and the two-groups model. *Statistical science*, 23(1):1–22.
- Fayed, H. and Atiya, A. (2014). An evaluation of the integral of the product of the error function and the normal probability density with application to the bivariate normal integral. *Mathematics of Computation*, 83(285):235–250.
- Flewelling, H. (2016). The Pan-STARRS 1 Medium Deep Field Variable Star Catalog. In *American Astronomical Society Meeting Abstracts #227*, volume 227 of *American Astronomical Society Meeting Abstracts*, page 144.25.
- Foreman-Mackey, D., Agol, E., Ambikasaran, S., and Angus, R. (2017). Fast and scalable Gaussian process modeling with applications to astronomical time series. *The Astronomical Journal*, 154(6):220.
- Genton, M. G. (2001). Classes of kernels for machine learning: a statistics perspective. *Journal of machine learning research*, 2(Dec):299–312.
- Georgelin, Y. M. and Georgelin, Y. P. (1976). The spiral structure of our Galaxy determined from H II regions. *Astronomy & Astrophysics*, 49:57–79.
- Gneiting, T. (2002). Compactly supported correlation functions. *Journal of Multivariate Analysis*, 83(2):493–508.
- Green, G. M., Schlafly, E. F., Finkbeiner, D., Rix, H.-W., Martin, N., Burgett, W., Draper, P. W., Flewelling, H., Hodapp, K., Kaiser, N., et al. (2018). Galactic reddening in 3d from stellar photometry—an improved map. *Monthly Notices of the Royal Astronomical Society*, 478(1):651–666.
- Green, G. M., Schlafly, E. F., Zucker, C., Speagle, J. S., and Finkbeiner, D. P. (2019). A 3d dust map based on gaia, pan-starrs 1 and 2mass. *arXiv preprint arXiv:1905.02734*.

- Heaton, M. J., Datta, A., Finley, A. O., Furrer, R., Guinness, J., Guhaniyogi, R., Gerber, F., Gramacy, R. B., Hammerling, D., Katzfuss, M., et al. (2019). A case study competition among methods for analyzing large spatial data. *Journal of Agricultural, Biological and Environmental Statistics*, 24(3):398–425.
- Hensman, J., Fusi, N., and Lawrence, N. D. (2013). Gaussian processes for big data. In *Proceedings of the Twenty-Ninth Conference on Uncertainty in Artificial Intelligence*, pages 282–290. AUAI Press.
- Hoffman, M. D., Blei, D. M., Wang, C., and Paisley, J. (2013). Stochastic variational inference. *The Journal of Machine Learning Research*, 14(1):1303–1347.
- Hopkins, P. F., Wetzel, A., Kereš, D., Faucher-Giguère, C.-A., Quataert, E., Boylan-Kolchin, M., Murray, N., Hayward, C. C., Garrison-Kimmel, S., and Hummels, C. (2018). FIRE-2 simulations: physics versus numerics in galaxy formation. *Monthly Notices of the Royal Astronomical Society*, 480(1):800–863.
- Jordan, M. I., Ghahramani, Z., Jaakkola, T. S., and Saul, L. K. (1999). An introduction to variational methods for graphical models. *Machine learning*, 37(2):183–233.
- Klypin, A., Kravtsov, A. V., Valenzuela, O., and Prada, F. (1999). Where Are the Missing Galactic Satellites? *The Astrophysical Journal*, 522(1):82–92.
- Krige, D. G. (1951). A statistical approach to some basic mine valuation problems on the witwatersrand. *Journal of the Southern African Institute of Mining and Metallurgy*, 52(6):119–139.
- Le, Q., Sarlós, T., and Smola, A. (2013). Fastfood-computing hilbert space expansions in loglinear time. In *International Conference on Machine Learning*, pages 244–252.
- Leike, R. and Enßlin, T. (2019). Charting nearby dust clouds using gaia data only. *arXiv preprint arXiv:1901.05971*.
- Matérn, B. (1960). Spatial variation: Stochastic models and their applications to some problems in forest surveys and other sampling investigations. *Meddelanden från Statens Skogsforskningsinstitut*, 49:1–144.
- Matheron, G. (1963). Principles of geostatistics. *Economic geology*, 58(8):1246–1266.
- Matheron, G. (1973). The intrinsic random functions and their applications. *Advances in applied probability*, 5(3):439–468.
- Mathis, J. S. (1990). Interstellar dust and extinction. *Annual Review of Astronomy and Astrophysics*, 28(1):37–70.
- Murray, I. and Adams, R. P. (2010). Slice sampling covariance hyperparameters of latent Gaussian models. In *Advances in neural information processing systems*, pages 1732–1740.
- Quiñonero-Candela, J. and Rasmussen, C. E. (2005). A unifying view of sparse approximate Gaussian process regression. *Journal of Machine Learning Research*, 6(Dec):1939–1959.
- Rahimi, A. and Recht, B. (2008). Random features for large-scale kernel machines. In *Advances in neural information processing systems*, pages 1177–1184.

- Rasmussen, C. E. and Williams, C. K. I. (2006). *Gaussian Processes for Machine Learning*. The MIT Press.
- Rezaei Kh., S., Bailer-Jones, C., Hanson, R., and Fouesneau, M. (2017). Inferring the three-dimensional distribution of dust in the galaxy with a non-parametric method-preparing for gaia. *Astronomy & Astrophysics*, 598:A125.
- Rezaei Kh., S., Bailer-Jones, C. A. L., Hogg, D. W., and Schultheis, M. (2018). Detection of the Milky Way spiral arms in dust from 3D mapping. *Astronomy & Astrophysics*, 618:A168.
- Robbins, H. and Monro, S. (1951). A stochastic approximation method. *The Annals of Mathematical Statistics*, 22(3):400–407.
- Rue, H., Martino, S., and Chopin, N. (2009). Approximate Bayesian inference for latent Gaussian models by using integrated nested Laplace approximations. *Journal of the royal statistical society: Series b (statistical methodology)*, 71(2):319–392.
- Sanderson, R. E., Wetzel, A., Loebman, S., Sharma, S., Hopkins, P. F., Garrison-Kimmel, S., Faucher-Giguère, C.-A., Kereš, D., and Quataert, E. (2018). Synthetic Gaia surveys from the FIRE cosmological simulations of Milky-Way-mass galaxies. *arXiv e-prints*, page arXiv:1806.10564.
- Schlegel, D. J., Finkbeiner, D. P., and Davis, M. (1998). Maps of dust infrared emission for use in estimation of reddening and cosmic microwave background radiation foregrounds. *The Astrophysical Journal*, 500(2):525.
- Snelson, E. and Ghahramani, Z. (2006). Sparse Gaussian processes using pseudo-inputs. In *Advances in neural information processing systems*, pages 1257–1264.
- Titsias, M. (2009). Variational learning of inducing variables in sparse Gaussian processes. In *Artificial Intelligence and Statistics*, pages 567–574.
- Wainwright, M. J., Jordan, M. I., et al. (2008). Graphical models, exponential families, and variational inference. *Foundations and Trends® in Machine Learning*, 1(1–2):1–305.
- Wetzel, A. R., Hopkins, P. F., hoon Kim, J., Faucher-Giguère, C.-A., Kereš, D., and Quataert, E. (2016). Reconciling Dwarf Galaxies with Λ CMD Cosmology: Simulating a Realistic Population of Satellites Around a Milky Way Mass Galaxy. *The Astrophysical Journal*, 827(2):L23.
- Yang, T., Li, Y.-F., Mahdavi, M., Jin, R., and Zhou, Z.-H. (2012). Nyström method vs random fourier features: A theoretical and empirical comparison. In *Advances in neural information processing systems*, pages 476–484.

Mapping Interstellar Dust with Gaussian Processes: Supplementary Material

A Covariance Function Definitions

We compare three families of covariance functions in this work: (i) squared exponential, (ii) Matérn, (iii) and a kernel from Gneiting (Gneiting, 2002). Each are parameterized with an amplitude scale σ^2 and length scale parameter ℓ .

The squared exponential kernel is defined

$$k(x, y) = \sigma^2 \exp\left(-\frac{1}{2\ell^2}|x - y|_2^2\right) \quad (29)$$

The Matern class of kernels

$$k(x, y) = \sigma^2 \frac{2^{1-\nu}}{\Gamma(\nu)} \left(\sqrt{2\nu} \frac{d}{\ell}\right)^\nu K_\nu\left(\sqrt{2\nu} \frac{d}{\ell}\right) \quad (30)$$

And the Gneiting kernel is defined

$$k(\tau) = \sigma^2 (1 + \tau^\alpha)^{-3} ((1 - \tau)\cos(\tau \cdot \pi) + (1/\pi)\sin(\tau \cdot \pi)) \quad (31)$$

for $\tau = |x - y|/\ell$, $\tau < 1$.

We graphically depict these covariance functions in Figure 8.

B Integrated Covariance Functions

Below is a simple derivation of the semi-integrated covariance function.

Claim B.1 (Semi-integrated Covariance Function). *The covariance between a process value $\rho_i \triangleq \rho(x_i)$ and an integrated value $e_j \triangleq \int_{x \in R_j} \rho(x) dx$ takes the form*

$$\text{Cov}(\rho_i, e_j) = \int_{x \in R_j} k(x_i, x) dx \quad (32)$$

$$= k^{(semi)}(x_i, x_j). \quad (33)$$

For consistency, we will write the integrated argument second.

Proof. Without loss of generality consider a mean zero process ρ . For positive and integrable covariance functions $k(\cdot, \cdot)$ (e.g. the Matérn and squared exponential) the double integral will be finite. By Fubini's theorem we can reverse the order of integration, yielding

$$\begin{aligned} \text{Cov}(\rho_i, e_j) &= \mathbb{E} \left[\rho_i \int_{x \in R_j} \rho(x) dx \right] \\ &= \mathbb{E} \left[\int_{x \in R_j} \rho_i \rho(x) dx \right] \\ &= \int_{x \in R_j} \mathbb{E} [\rho_i \rho(x)] dx \\ &= \int_{x \in R_j} \text{Cov}(\rho_i, \rho(x)) dx = \int_{x \in R_j} k(x_i, x) dx. \end{aligned}$$

□

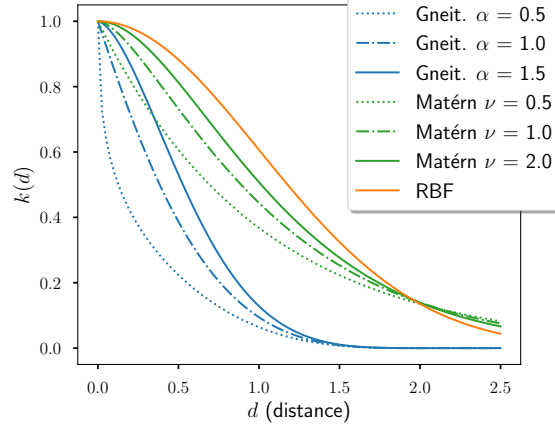


Figure 8: Correlation function for squared exponential, Matérn, and Gneiting kernels. Here the squared exponential and Matérn kernels have $\sigma^2 = 1$ and $\ell = 1$; the Gneiting kernel has $\ell = 2$. Note that the Gneiting kernel goes to zero above ℓ , while the other two kernels. Further, the steepness of the function at 0 determines how smooth the GP sample paths will be — the squared exponential kernel is the smoothest, while the Gneiting $\alpha = .5$ is the most jagged.

B.1 Semi-integrated Squared exponential kernel

The *squared exponential* covariance function is commonly used for Gaussian process regression (Rasmussen and Williams, 2006). For D -dimensional inputs x_i, x_j , it is

$$k_{sqe}(x_i, x_j) = \sigma^2 \exp\left(-\frac{1}{2}(x_i - x_j)^\top L^{-1}(x_i - x_j)\right), \quad (34)$$

where $\theta = (L, \sigma^2)$ are the $D \times D$ -size length scale matrix L and the process marginal variance σ^2 . For an isotropic Gaussian process, the length scale matrix L is $\ell \cdot I_D$ for a scalar length scale ℓ . The length scale controls the smoothness of the function; smaller length scales create more wiggly functions and longer length scales create more slowly-changing functions. This kernel puts support on functions with infinitely differentiable sample paths.

The squared exponential kernel admits an analytically tractable form for the semi-integrated kernel

$$k_{sqe}^{(\text{semi})}(x_i, x_j) = \int_{[0,1]} k_{sqe}(x_i, \alpha \cdot x_j) \|x_j\|_2 d\alpha \quad (35)$$

$$= \frac{1}{2} \|x_j\|_2 \sigma^2 \sqrt{\frac{2\pi}{a}} \exp\left(\frac{b^2}{2a} - \frac{c}{2}\right) \left[\operatorname{erf}\left(\frac{1-b/a}{\sqrt{2/a}}\right) - \operatorname{erf}\left(\frac{-b/a}{\sqrt{2/a}}\right) \right] \quad (36)$$

where $\operatorname{erf}(\cdot)$ is the error function, and a, b , and c are defined

$$a = x_j^\top L^{-1} x_j, \quad b = x_i^\top L^{-1} x_j, \quad c = x_i^\top L^{-1} x_i$$

and the origin, or observer, is at 0.

The doubly-integrated squared exponential covariance function is not as straightforward to express. Deriving the doubly-integrated squared exponential covariance function requires integrating the expression in Equation (36). Integrating the error function multiplied by a quadratic requires either numerical approximation or a more sophisticated approach (Fayed and Atiya, 2014). We

Algorithm 1: Exact Gaussian process inference with noisy integrated observations.

Data: data set $\mathcal{D} \triangleq \{x_n, \sigma_n, a_n\}_{n=1}^N$, test location x_* , covariance functions: standard $k(\cdot, \cdot)$, semi-integrated $k^{(\text{semi})}(\cdot, \cdot)$, and doubly-integrated $k^{(\text{double})}(\cdot, \cdot)$

Result: μ_*, σ_*^2 for posterior $p(\rho(x_*)|\mathcal{D}) = \mathcal{N}(\mu_*, \sigma_*^2)$

$(\mathbf{K}_e)_{i,j} \leftarrow k^{(\text{double})}(x_i, x_j)$ for $i, j = 1, \dots, N$; // doubly-integrated Gram matrix

$(\mathbf{K}_{*,e})_{*,j} \leftarrow k^{(\text{semi})}(x_*, x_j)$ for $j = 1, \dots, N$; // semi-integrated cross covariance

$K_{*,*} \leftarrow k(x_*, x_*)$; // prior variance from standard covariance function

$\Sigma \leftarrow \text{diag}(\sigma_1^2, \dots, \sigma_N^2)$

$\mu_* \leftarrow \mathbf{K}_{*,e}(\mathbf{K}_e + \Sigma)^{-1}\mathbf{a}$

$\sigma_*^2 \leftarrow K_{*,*} - \mathbf{K}_{*,e}(\mathbf{K}_e + \Sigma)^{-1}\mathbf{K}_{*,e}^\top$

return μ_*, σ_*^2

note that, while it is straightforward to analytically derive the integral of the squared exponential kernel over the *unbounded region* $[-\infty, \infty]^2$ (e.g. to compute a Gaussian normalizing constant), it is not straightforward to integrate over two-dimensional compact sets, e.g. $[0, x_i] \times [0, x_j]$ — this is exactly what is required to compute the doubly-integrated kernel.

C Stochastic Natural Gradients for SVGPs

Following [Hensman et al. \(2013\)](#) and [Hoffman et al. \(2013\)](#), the natural gradient for variational parameters $\boldsymbol{\lambda} = \mathbf{m}_\lambda, \mathbf{S}_\lambda$ is straightforward to express using the natural parameterization of the multivariate normal q_λ

$$\boldsymbol{\eta}_1 = \mathbf{S}_\lambda^{-1}\mathbf{m}_\lambda, \quad \boldsymbol{\eta}_2 = -\frac{1}{2}\mathbf{S}_\lambda^{-1}. \quad (37)$$

The natural gradient of \mathcal{L} with respect to $\boldsymbol{\eta}_1$ and $\boldsymbol{\eta}_2$ can be written

$$\tilde{\nabla}_{\boldsymbol{\eta}_2}\mathcal{L} = -\frac{1}{2}\Lambda + \boldsymbol{\eta}_2 \quad (38)$$

$$\tilde{\nabla}_{\boldsymbol{\eta}_1}\mathcal{L} = -\frac{1}{2}\mathbf{K}_{\mathbf{u},\mathbf{u}}^{-1}\tilde{\mathbf{K}}_{\mathbf{u},\rho}\mathbf{y} + \boldsymbol{\eta}_1 \quad (39)$$

where we define

$$\Lambda = \mathbf{K}_{\mathbf{u},\mathbf{u}}^{-1}\tilde{\mathbf{K}}_{\mathbf{u},\rho}\tilde{\mathbf{K}}_{\rho,\mathbf{u}}\mathbf{K}_{\mathbf{u},\mathbf{u}}^{-1} + \mathbf{K}_{\mathbf{u},\mathbf{u}}^{-1} \quad (40)$$

$$= \sum_n \mathbf{K}_{\mathbf{u},\mathbf{u}}^{-1} \left(\tilde{\mathbf{K}}_{\mathbf{u},n}\tilde{\mathbf{K}}_{n,\mathbf{u}} \right) \mathbf{K}_{\mathbf{u},\mathbf{u}}^{-1} + \mathbf{K}_{\mathbf{u},\mathbf{u}}^{-1}, \quad (41)$$

and

$$\tilde{\mathbf{K}}_{\rho,\mathbf{u}} \triangleq \Sigma^{-1/2}\mathbf{K}_{\rho,\mathbf{u}} \quad (42)$$

$$(\mathbf{K}_{\rho,\mathbf{u}})_{n,m} = k(x_n, \bar{x}_m) \quad (43)$$

$$\Sigma \triangleq \text{diag}(\sigma_1^2, \dots, \sigma_N^2). \quad (44)$$

Note that Equation 41 shows that the term Λ can be decomposed into a sum of N data-specific terms. Further, the gradient for $\boldsymbol{\eta}_1$ includes the term $\tilde{\mathbf{K}}_{\mathbf{u},\rho}\mathbf{y} = \sum_n \tilde{\mathbf{K}}_{\mathbf{u},n}y_n$ that also decomposes

into a sum over the N data-specific terms. These two decompositions enable us to compute unbiased mini-batched natural gradients and optimize the ELBO using stochastic gradient ascent. An additional benefit of using the natural gradient is that a stochastic gradient update to η_2 will stay in the positive semi-definite cone. This allows us to directly parameterize η_2 and not its Cholesky factor or symmetric square root, simplifying our implementation.

D Whitened Parameterization Gradients

The relationship between the whitened model over \mathbf{z} and the standard model over \mathbf{u} implies the following relationship between the Gaussian variational parameters

$$\mathbf{m} = \mathbf{L}\tilde{\mathbf{m}} \quad (45)$$

$$\mathbf{S} = \mathbf{L}\tilde{\mathbf{S}}\mathbf{L}^\top. \quad (46)$$

Similarly, the natural parameters have the relationship

$$\eta_1 = \mathbf{S}^{-1}\mathbf{m} = (\mathbf{L}^\top)^{-1}\tilde{\mathbf{S}}^{-1}\mathbf{L}^{-1}\mathbf{L}\tilde{\mathbf{m}} = (\mathbf{L}^\top)^{-1}\tilde{\eta}_1 \quad (47)$$

$$\eta_2 = -\frac{1}{2}\mathbf{S}^{-1} = -\frac{1}{2}(\mathbf{L}^\top)^{-1}\tilde{\mathbf{S}}^{-1}\mathbf{L}^{-1} = (\mathbf{L}^\top)^{-1}\tilde{\eta}_2\mathbf{L}^{-1}. \quad (48)$$

The natural gradient is invariant to parameterization (Amari, 1982), which implies that the whitened natural gradient transformation can be derived by multiplying the standard update by \mathbf{L}^\top

$$\eta_1^{(t+1)} = \eta_1^{(t)} + (\boldsymbol{\mu} - \eta_1^{(t)}) \quad \text{natural gradient updates} \quad (49)$$

$$\eta_2^{(t+1)} = \eta_2^{(t)} + \left(-\frac{1}{2}\Lambda - \eta_1^{(t)}\right) \quad (50)$$

$$\implies \tilde{\eta}_1^{(t+1)} = \tilde{\eta}_1^{(t)} + (\mathbf{L}^\top\boldsymbol{\mu} - \tilde{\eta}_1^{(t)}) \quad \text{whitened natural gradient updates} \quad (51)$$

$$\tilde{\eta}_2^{(t+1)} = \tilde{\eta}_2^{(t)} + \left(-\frac{1}{2}\mathbf{L}^\top\Lambda\mathbf{L} - \tilde{\eta}_2^{(t)}\right). \quad (52)$$

This yields a natural interpretation — the whitened sufficient statistics must undo the inverse covariance structure from the prior before updating the variational parameters.⁶

When it comes time to predict, we will simply transform the whitened parameters into standard parameters using Equation 46, and proceed with the usual multivariate Gaussian conditioning. In Section G.1 we show that optimizing in the whitened space can yield better tuned covariance function parameters. This empirical evidence supports the practical conclusion that jointly tuning the variational approximation over \mathbf{z} and $\boldsymbol{\theta}$ is an easier optimization problem than jointly tuning parameters over \mathbf{u} and $\boldsymbol{\theta}$ due to the stronger dependence between \mathbf{u} and $\boldsymbol{\theta}$.

E Scaling Integrated Observation GPs: Algorithm Details

E.1 Monte Carlo estimators for semi-integrated kernels

For tractable semi-integrated covariance functions (e.g. the squared exponential kernel) we can easily substitute a closed form computation for $\mathbf{K}_{\rho,\mathbf{u}}$ in Equation 39. However, when the semi-integrated covariance term is intractable, directly using natural gradient updates becomes complicated. One approach is to use numeric integration — the semi-integrated covariance is a

⁶Note that the natural parameters are in “information form” — pre- and post-multiplying by the covariance Cholesky will whiten a precision matrix.

one-dimensional integral that can be approximated with quadrature techniques. However, when we have N and M very large, solving $N \times M$ numerical integration problems to populate the cross covariance matrix can be too expensive to be practical.

Stochastic natural gradient updates employ computationally cheap estimates of the true gradient to solve the original optimization problem. The operative question is, how *good* do these estimates have to be to effectively find the optimal solution?

Similarly, numeric integration approximations to $k^{(semi)}(\cdot, \cdot)$ are precise to nearly machine precision, but are computationally expensive. Analogously we can ask, how *good* do the semi-integrated covariance approximations have to be to effectively find the optimal solution?

Pursuing this idea, we propose using a Monte Carlo approximation to the semi-integrated covariance values — we sample uniformly along the integral path and average the original covariance values. More formally, we introduce a uniform random variable ν_{R_n} that takes values along the ray R_n from the origin to x_n . We can now write the semi-integrated covariance as

$$k^{(semi)}(x_m, x_n) = \int_{x \in R_n} k(x_m, x) dx \quad (53)$$

$$= |R_n| \int_{\nu \in R_n} \underbrace{\frac{1}{|R_n|}}_{=p(\nu)} k(x_m, x) dx \quad (54)$$

$$= |R_n| \mathbb{E}_\nu [k(x_m, \nu)] . \quad (55)$$

This form admits a simple Monte Carlo estimator

$$\nu^{(1)}, \dots, \nu^{(L)} \sim \text{Unif}(R_n) \quad (56)$$

$$\hat{k}^{(semi)}(x_m, x_n) = \frac{|R_n|}{L} \sum_{\ell} k(x_m, \nu^{(\ell)}) . \quad (57)$$

It is straightforward to show that Equation 57 is an unbiased and consistent estimator for the true semi-integrated covariance value evaluated at x_m and x_n .

Uniformly distributed grids The unbiased Monte Carlo estimator $\hat{k}^{(semi)}$ will have some variance about the mean. The quality of an unbiased estimator is often measured by how low its variance is — the more precise the better. Independent and identically distributed samples $\nu^{(\ell)}$ will yield the correct expectation, but may be lower variance than a more clever sampling scheme. For our application, we uniformly sample along the ray that traces from the origin O to the observation location x_n . Intuitively, drawing two uniform random variables that are very close to one another will carry redundant information (for smooth functions $k(\cdot, \cdot)$). Spreading our samples out to cover more of the length of the ray may yield more precise estimates, provided that we can construct a sample that yields the correct expectation.

One inexpensive way to generate a set of identically distributed (but not independent samples) is to lay down a random grid of points. Consider the sampling procedure for L samples along the unit interval

$$\nu^{(1)} \sim \text{Unif}(0, 1/L) \quad (58)$$

$$\nu^{(\ell)} = \nu^{(\ell-1)} + \frac{1}{L} \quad \text{for } \ell = 2, \dots, L. \quad (59)$$

This sampling scheme will generate a set of L correlated samples that constructs a randomly placed grid within the unit interval. If we randomly permute the variables ν_1, \dots, ν_L (or, equivalently, randomly select one of them) then the marginal distribution of the random variable will

be $Unif(0, 1)$ — this ensures that the expectation of the estimator in Equation 25 will remain unbiased. However, because the samples are anti-correlated, the variance of the estimator can be substantially reduced.

Biased gradient estimates The Monte Carlo estimate of $\hat{k}^{(semi)}(x_m, x_n)$ is unbiased, but non-linear functions of an unbiased estimator, in general, may jettison this property. In our application, the goal is to compute cheap, unbiased estimates of the gradient of the variational parameters \mathbf{m}, \mathbf{S} (or their information form parameterization $\boldsymbol{\eta}_1, \boldsymbol{\eta}_2$).

For a single term n , the gradient for η_1 is a linear function of the semi-integrated covariance vector $\mathbf{K}_{n,\mathbf{u}} = [k^{(semi)}(x_n, x_1), \dots, k^{(semi)}(x_n, x_M)]$.⁷ Due to this linearity, plugging in an unbiased estimator, $\hat{\mathbf{K}}_{n,\rho}$, for $\mathbf{K}_{n,\mathbf{u}}$ will form an unbiased gradient estimate for $\tilde{\nabla}_{\eta_1} \mathcal{L}$. However, plugging in $\hat{\mathbf{K}}_{n,\mathbf{u}}$ into the gradient term for η_2 will form a non-linear function of an unbiased estimator, resulting in a biased estimate of $\tilde{\nabla}_{\eta_2}$.

To see this, consider the vector of unbiased estimates of the semi-integrated covariance

$$\hat{\mathbf{K}}_{n,\rho} = [\hat{k}^{(semi)}(x_1, x_n), \dots, \hat{k}^{(semi)}(x_m, x_n)]. \quad (60)$$

The stochastic component of the gradient for η_2 can be written

$$\mathbb{E} [\mathbf{K}_{\mathbf{u},\mathbf{u}}^{-1} \mathbf{K}_{\mathbf{u},n} \mathbf{K}_{n,\mathbf{u}} \mathbf{K}_{\mathbf{u},\mathbf{u}}^{-1}] = \mathbf{K}_{\mathbf{u},\mathbf{u}}^{-1} \mathbb{E} [\mathbf{K}_{\mathbf{u},n} \mathbf{K}_{n,\mathbf{u}}] \mathbf{K}_{\mathbf{u},\mathbf{u}}^{-1} \quad (61)$$

where $\mathbf{K}_{\mathbf{u},\mathbf{u}}^{-1}$ can be computed exactly, leaving the expectation of the outer product of the semi-integrated covariance terms $\mathbb{E} [\mathbf{K}_{\mathbf{u},n} \mathbf{K}_{n,\mathbf{u}}]$. Given an unbiased estimator for $\mathbf{K}_{n,\mathbf{u}}$ the naive plugin estimate for $\mathbf{K}_{n,\mathbf{u}} \mathbf{K}_{\mathbf{u},n}$ is

$$\hat{O}^{(plugin)} = \hat{\mathbf{K}}_{\mathbf{u},n} \hat{\mathbf{K}}_{n,\mathbf{u}} \quad (62)$$

which is *biased* in general

$$\mathbb{E} [\hat{\mathbf{K}}_{\mathbf{u},n} \hat{\mathbf{K}}_{n,\mathbf{u}}] \neq \mathbb{E} [\hat{\mathbf{K}}_{\mathbf{u},n}] \mathbb{E} [\hat{\mathbf{K}}_{n,\mathbf{u}}] = \mathbf{K}_{n,\mathbf{u}} \mathbf{K}_{n,\mathbf{u}}^\top. \quad (63)$$

Fortunately, we can construct an unbiased estimator for this outer product. Note that the outer product of an expectation can be expressed as

$$\mathbb{E} [\mathbf{x}] \mathbb{E} [\mathbf{x}]^\top = \mathbb{E} [\mathbf{x}\mathbf{x}^\top] - \text{Cov}(\mathbf{x}) \quad (64)$$

Given an L -size sample $\mathbf{x}_1, \dots, \mathbf{x}_L$ we can compute unbiased estimators for $\mu = \mathbb{E}[\mathbf{x}]$, $M \triangleq \mathbb{E} [\mathbf{x}\mathbf{x}^\top]$, and $\Sigma \triangleq \text{Cov}(\mathbf{x})$

$$\hat{\mu} = \frac{1}{L} \sum_{\ell} \mathbf{x}_{\ell} \quad (65)$$

$$\hat{\Sigma} = \frac{1}{L-1} \sum_{\ell} (\mathbf{x}_{\ell} - \hat{\mu})(\mathbf{x}_{\ell} - \hat{\mu})^\top \quad (66)$$

$$\hat{M} = \frac{1}{L} \sum_{\ell} \mathbf{x}_{\ell} \mathbf{x}_{\ell}^\top \quad (67)$$

With these estimators, $\hat{M} - \hat{\Sigma}$ forms an unbiased estimate for $\mathbb{E}[\mathbf{x}]\mathbb{E}[\mathbf{x}]^\top$

$$\mathbb{E} [\hat{M} - \hat{\Sigma}] = \mathbb{E}[\mathbf{x}]\mathbb{E}[\mathbf{x}]^\top. \quad (68)$$

⁷Note that the order of the subscripts indicates the vector dimensions, e.g. $\mathbf{K}_{n,\mathbf{u}} \in \mathbb{R}^{1 \times M}$ and $\mathbf{K}_{n,\mathbf{u}}^\top = \mathbf{K}_{\mathbf{u},n} \in \mathbb{R}^{M \times 1}$.

Algorithm 2: Scalable integrated observation GP inference with mini-batches and Monte Carlo semi-integrated covariance estimates. The natural gradient estimator uses L Monte Carlo samples to approximate the semi-integrated covariance and B data observations to approximate the complete data objective.

Data: $\mathcal{D} \triangleq \{a_n, x_n, \sigma_n^2\}_{n=1}^N$ (data), $k^{(\theta)}(\cdot, \cdot)$ (covariance function); $(\boldsymbol{\lambda}^{(0)}, \boldsymbol{\theta}^{(0)})$ (initial values); $k(\cdot, \cdot)$ (covariance function); $(\Delta_{\boldsymbol{\lambda}}, \Delta_{\boldsymbol{\theta}})$ (step-sizes); B (batch size); L (Monte Carlo semi-integrated estimator sample size);

Result: $\boldsymbol{\lambda}, \boldsymbol{\theta}$ variational and covariance function parameters

$\hat{k}^{(dd)}(\cdot) \leftarrow \text{Interpolate-Doubly-Diag}(k^{(\theta_0)}(\cdot, \cdot));$ // construct diagonal interpolator

for $t \leftarrow 1$ **to** t_{max} **do**

$\mathcal{D}_t \leftarrow \text{Batch}(\mathcal{D}, B);$ // mini-batch of data

$\boldsymbol{\lambda}^{(t)} \leftarrow \boldsymbol{\lambda}^{(t-1)} + \Delta_{\boldsymbol{\lambda}} \cdot \tilde{\nabla}_{\boldsymbol{\lambda}}^{(MC)} \mathcal{L}(\boldsymbol{\lambda}^{(t-1)}, \boldsymbol{\theta}^{(t-1)}, \mathcal{D}_t, L);$ // MC natural grad update

$\boldsymbol{\theta}^{(t)} \leftarrow \boldsymbol{\theta}^{(t-1)} + \Delta_{\boldsymbol{\theta}} \cdot \nabla_{\boldsymbol{\theta}}^{(MC)} \mathcal{L}(\boldsymbol{\lambda}^{(t-1)}, \boldsymbol{\theta}^{(t-1)}, \mathcal{D}_t, L, \hat{k}^{(dd)}(\cdot));$ // MC kernel grad update

$\text{sgd-update}(\boldsymbol{\lambda}^{(t)}, \tilde{\nabla} \boldsymbol{\lambda}^{(MC)});$ // gradient-based update

end

return $\boldsymbol{\lambda}^{(t_{max})}, \boldsymbol{\theta}^{(t_{max})};$ // optimal parameters

We can use this fact to construct a de-biased estimator for O

$$\hat{O}^{(unbiased)} = \hat{M} \left(\{\hat{\mathbf{K}}_{n,\mathbf{u}}^{(\ell)}\}_{\ell=1}^L \right) - \hat{\Sigma} \left(\{\hat{\mathbf{K}}_{n,\mathbf{u}}^{(\ell)}\}_{\ell=1}^L \right). \quad (69)$$

Though $\hat{M} - \hat{\Sigma}$ forms an unbiased and symmetric estimator of the outer product, this estimator may not be positive semi-definite. If this estimator is not positive semi-definite, then a gradient step along this direction may take the optimization routine outside of the PSD cone. To ensure safe gradient updates, we will have to meticulously track the magnitude of the lowest eigenvalues of this matrix.

Though biased, the naive plugin estimator in Equation 62 will always be non-negative definite, resulting in gradient updates that are guaranteed to remain in the PSD cone. Proceeding with this estimator, we must ask, how much bias is too much bias? We explore this question empirically in Section F, comparing the optimization traces of algorithms using various sample sizes L to the exact $k^{(semi)}(\cdot, \cdot)$ values in the squared exponential kernel case. We see that, though biased, this gradient estimator can closely approximate the performance of the exact semi-integrated kernel given a modest number of samples (≈ 20).

Monte Carlo SVGP comparison

The squared exponential kernel admits an analytic form for the semi-integrated covariance function. This gives us a way to directly compare our Monte Carlo semi-integrated approximation within SVGP to the same algorithm using exact semi-integrated covariance values. In this experiment, we compare the progress of the exact variational objective throughout optimization using different gradient estimators — the analytic version, and the biased Monte Carlo gradients using sample size $L = 5, 7, 10, 20$, and 50.

We fit variational parameters using stochastic natural gradient descent with mini-batches of size 1,000 and step size 0.1. We fix the covariance function parameters in this experiment to report

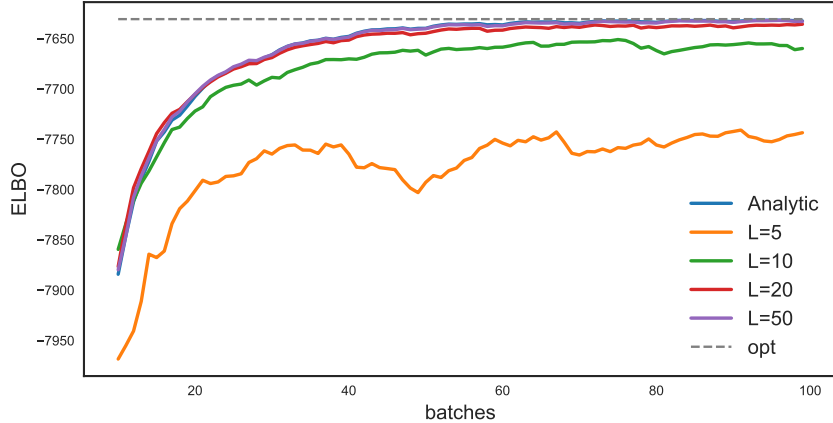


Figure 9: Monte Carlo estimates of semi-integrated covariance functions enable efficient ELBO inference competitive with the analytic semi-integrated covariance. Above is a comparison of ELBO traces by mini-batch (x -axis) for the squared exponential kernel. The analytic semi-integrated kernel was used in blue (hidden behind the $L = 50$ purple line. The optimal value is depicted with the dotted gray line.

a more direct comparison between exact and Monte Carlo gradients — in subsequent experiments we apply gradient updates to these two parameters as well. Inducing points are placed on a fixed grid of size 20×20 ($M = 400$), tiling the 2-d space.

At each batch, we compute the complete-data ELBO objective (using the exact squared exponential semi-integrated covariance function across methods). Additionally, we compute the optimal value of the ELBO (by solving for the optimal values of \mathbf{m}_λ and \mathbf{S}_λ in closed form — an operation that is too costly when N is on the order of millions of observations) which we depict alongside optimization traces.

Figure 9 compares the progress of optimizers using different gradient estimators. The “analytic” version uses the closed form semi-integrated covariance, while the Monte Carlo runs use sample sizes of varying values. We see that with as few as $L = 20$ samples the resulting optimization routine very nearly finds the optimal value (depicted in grey), and almost exactly matches the path of the “analytic” routine. This confirms that these Monte Carlo semi-integrated covariance estimators are suitable plug-in estimators for fitting models with covariance functions that do not admit an analytic form for the semi-integrated covariance, (e.g. the Gneiting and Matérn kernels).

E.2 Fast doubly-integrated kernel diagonal interpolation

Approximating doubly-integrated diagonal terms To make predictions within the SVGP framework, we need to compute the marginal variance of each observation according to the Gaussian process prior. Concretely, this amounts to computing the $\mathbf{K}_{*,*}$ term in Equation 81. In the integrated observation setting, this requires computing the variance of an integrated observation

$$(\tilde{\mathbf{K}}_N)_{n,n} = Cov(a_n, a_n) = Var(e_n) = Var \left(\int_{[0,1]} \rho(\alpha \cdot x_n) d\alpha \right). \quad (70)$$

This marginal variance corresponds to the diagonal of the doubly-integrated kernel and may not be analytically tractable. For the squared exponential kernel, this would require integrating the

semi-integrated kernel expressed in Equation 36 over a compact set, which does not yield a closed form (Fayed and Atiya, 2014).

Fortunately, for a one-dimensional compact set, this integral can be numerically computed relatively efficiently. Unfortunately, if we are scaling to millions of observations, we will have to perform millions of numerical integrations to simply evaluate the likelihood of the data under one setting of the covariance function parameters. Further, we will have to recompute all of these numerical integrations at each iteration when fitting covariance function parameters (or computing their posterior).

The inducing point variance correction method requires only computing the marginal variance of each integrated observation under the prior. For stationary kernels this is a function only of the distance of the observation to the origin (or more generally, the length of the integrated ray). Similar to the semi-integrated kernel, we can see that this is true by expanding the stationary kernel

$$\int_0^1 k(|x - \alpha x|) d\alpha = \int_0^1 k((x^\top x + \alpha^2 x^\top x - 2\alpha x^\top x)^{1/2}) d\alpha \quad (71)$$

$$= \int_0^1 k((|x|^2 + \alpha^2 |x|^2 - 2\alpha |x|^2)^{1/2}) d\alpha \quad (72)$$

$$= f(|x|). \quad (73)$$

Due to this stationarity, we can view each numerical computation as evaluating the function $k_\theta(\mathbf{d}_n) = \tilde{K}_n n$ where \mathbf{d}_n is the distance of observation \mathbf{x}_n from the origin. This perspective suggests a numerically cheap approximation — simply estimate this function along a fixed grid of distances (that spans the range of observed distances) and interpolate the value for each observation.

This one-dimensional function can be estimated independent of the length scale parameter for isotropic and stationary covariance functions. The effect of the length scale parameter is to effectively redefine distance, or the magnitude of $|x|$. We can account for this change by re-scaling the $|x|$ distance and multiplying the result by ℓ . Specifically for the diagonal, this becomes simply a function of a one-dimensional distance, which can easily be interpolated with a small number of knots.

Making predictions. To estimate the process value ρ_* at new location x_* , we use the posterior predictive distribution $p(\rho_* | \mathcal{D})$. Within the SVGP framework, we approximate this distribution using the posterior $q_\lambda(\mathbf{u})$

$$p(\rho_* | \mathcal{D}) = \int p(\rho_* | \mathbf{u}) p(\mathbf{u} | \mathcal{D}) d\mathbf{u} \quad (74)$$

$$\approx \int p(\rho_* | \mathbf{u}) q_\lambda(\mathbf{u}) d\mathbf{u} . \quad (75)$$

Under the approximation, \mathbf{u} and ρ_* are jointly normal, making this predictive distribution available in closed form

$$p(\rho_* | \mathcal{D}) = \mathcal{N}(\mu_*, \sigma_*^2) \quad (76)$$

$$\mu_* = \mathbf{K}_{*,\mathbf{u}} \mathbf{K}_{\mathbf{u},\mathbf{u}}^{-1} \mathbf{m} \quad (77)$$

$$\sigma_*^2 = \tilde{\mathbf{K}}_{*,*} + \mathbf{K}_{*,\mathbf{u}} \mathbf{K}_{\mathbf{u},\mathbf{u}}^{-1} \mathbf{S} \mathbf{K}_{\mathbf{u},\mathbf{u}}^{-1} \mathbf{K}_{\mathbf{u},*} \quad (78)$$

where

$$(\mathbf{K}_{*,\mathbf{u}})_m = \text{Cov}(\rho_*, \mathbf{u}_m) \quad (79)$$

$$\mathbf{K}_{*,*} = \text{Var}(\rho_*) \quad (80)$$

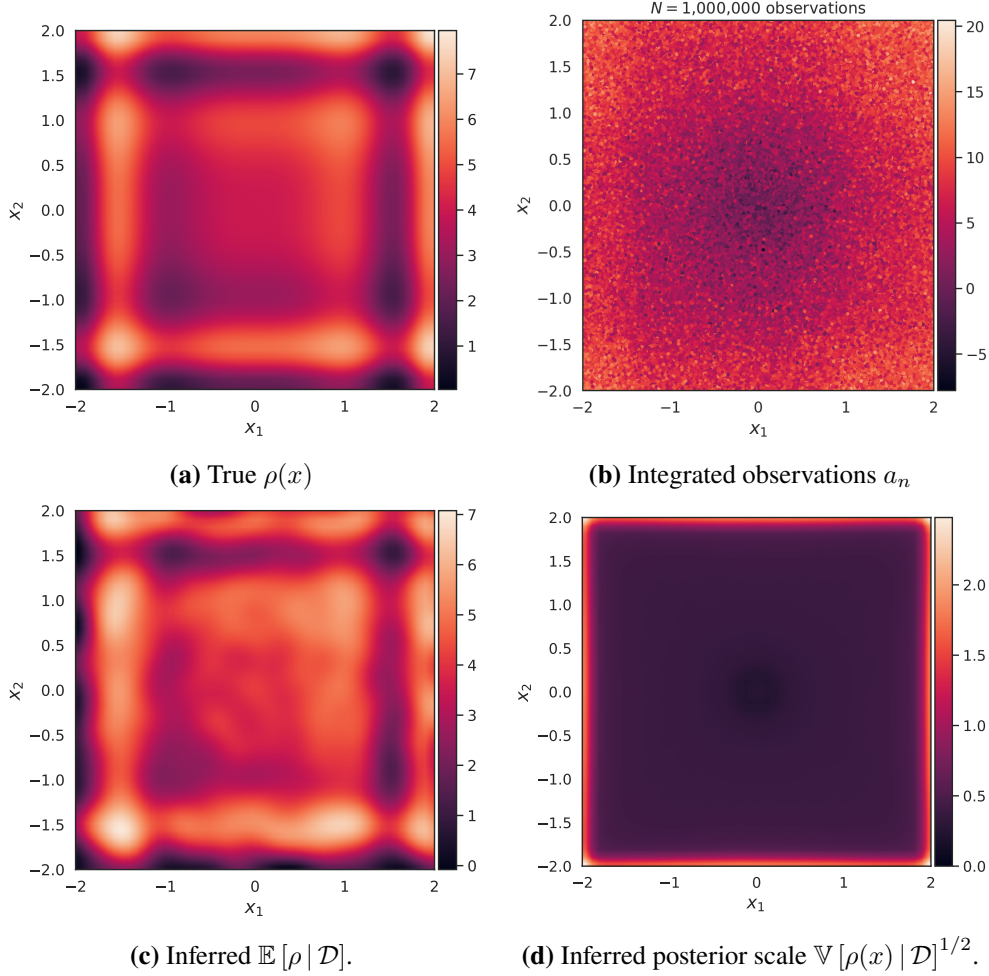


Figure 10: Integrated observation GPs can reveal spatial structure from a severely limited vantage point. This figure summarizes synthetic data posterior inference using $N = 1,000,000$ examples in a two-dimensional space. Panel 10a depicts the true (unobserved) $\rho(x)$ that generates the data. Panel 10b depicts the observed data, noisy integrated measurements of ρ from the origin to uniformly random points in the square. 10c depicts the inferred ρ given these observations using ZIGGY with a squared exponential kernel. 10d depicts the marginal posterior standard deviation at each location in \mathcal{X} -space.

$$\tilde{\mathbf{K}}_{*,*} \triangleq \mathbf{K}_{*,*} - \mathbf{K}_{*,\mathbf{u}} \mathbf{K}_{\mathbf{u},\mathbf{u}}^{-1} \mathbf{K}_{\mathbf{u},*}. \quad (81)$$

Prediction for integrated process values, $e_* = \int_{x \in R_*} \rho(x) dx$, can be computed similarly by substituting semi-integrated covariance values into the vector $\mathbf{K}_{*,\mathbf{u}}$ and the doubly integrated covariance value $\mathbf{K}_{*,*}$.

F Validation on Synthetic Data

In this section we study the performance of ZIGGY on synthetic data under varying conditions. To empirically evaluate ZIGGY we measure the quality of its statistical inferences on a two-dimensional synthetic example. To generate synthetic data, we first define the unobserved $\rho : \mathbb{R}^2 \mapsto \mathbb{R}$ and

generate noise with known variance. The form we chose for ρ is

$$\rho(x) = 4 + \sum_{d=1}^d x_d \cdot \sin(2x_d^2), \quad (82)$$

which is visualized in Figure 10a. This test function has clear regions of high density far from the observation point (e.g. around $x = (-1.5, -1.5)$) and it is positive everywhere. We generate a dataset of N noisy integrated observations

$$x_n \sim \text{Unif}(\mathcal{X}) \quad \text{simulated star locations} \quad (83)$$

$$e_n = \int_{x \in R_n} \rho(x) dx \quad \text{simulated extinctions} \quad (84)$$

$$a_n \sim \mathcal{N}(e_n, \sigma_n^2) \quad \text{noisy integrated observation} \quad (85)$$

where the domain is $\mathcal{X} = [-2, 2]^2$, and the noise variance is chosen to be $\sigma_n^2 = 4$ to roughly approximate the noise level of extinction measurements. The true extinctions, e_n , are computed to high precision using numerical quadrature, integrating from the origin to the random location x_n . The integrated observations are depicted in Figure 10b. We estimate this synthetic $\rho(\cdot)$ from noisy integrated observations using the approach developed in the previous section. In this experiment, we fix a grid of 20×20 inducing points, evenly spaced from $[-2, 2]$ in each of the two dimensions.

In Section F.1, the first set of simulations compares posterior estimates of $\rho(\cdot)$ as a function of training data set size. Posterior estimates continue to become more accurate and well-calibrated even as the number of integrated observation N grows from one hundred thousand to one million. This accuracy highlights the importance of scaling inference to more observations in order to obtain a more accurate statistical estimator.

In Section F.2, we compare posterior estimate quality with a fixed dataset over different kernels, each encoding different assumptions about the underlying function. This experiment tests the Monte Carlo approach that can incorporate kernels that do not admit an analytic form for the semi-integrated kernel. Finally, Appendix G describes additional synthetic experiments that examine the effect of two algorithm hyper parameter choices on variational objective optimization, the whitened parameterization and the number of Monte Carlo semi-integrated covariance samples.

A python and PyTorch implementation is available.⁸ Code to reproduce experiments are included in the repository.

F.1 The quality of the estimate

We study the quality of the estimate of $\rho(x)$ as a function of data set size N . We fit the dust model to synthetic observations with data set sizes $N \in \{10^3, 10^4, 10^5, 10^6\}$. We measure model quality by computing root mean squared error (RMSE) and log likelihood (LL) on a set of $N_{\text{test}} = 2,000$ held out extinction values

$$\text{RMSE} = \left(\frac{1}{N_{\text{test}}} \sum_{n=1}^{N_{\text{test}}} (\mathbb{E}[e_* | \mathcal{D}] - e_*)^2 \right)^{1/2} \quad (86)$$

$$\text{LL} = \frac{1}{N_{\text{test}}} \sum_{n=1}^{N_{\text{test}}} \ln p(e_n | \mathcal{D}) . \quad (87)$$

⁸Available at [REDACTED TO PRESERVE AUTHOR BLINDNESS].

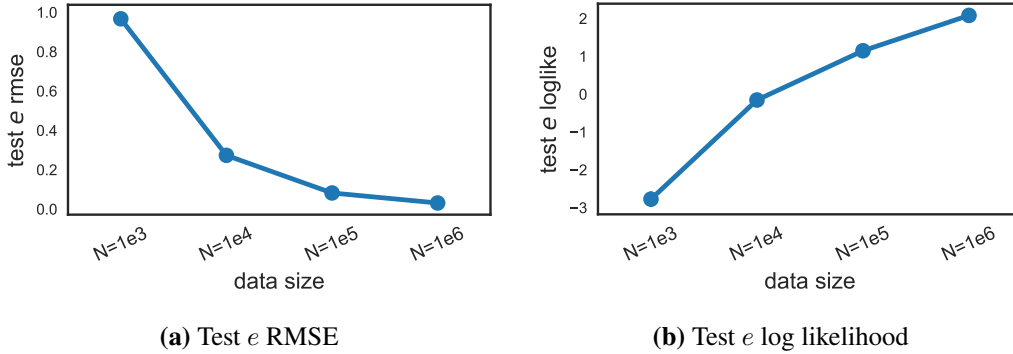


Figure 11: Scaling to massive N improves estimator performance. Above, we compare predictive RMSE (left) and log likelihood (right) as a function of data set size N on a held out sample of test stars.

Each model uses $M = 20 \times 20$ inducing points, evenly spaced in a grid in the input space. We trained each model until convergence, using batches of size 1,000, a step size of $1e-3$ and a kernel parameter step size of $1e-6$. (Additional optimization details can be found in the implementation.)

Figure 10 summarizes the model’s fit using one million observations, the most we tried in this example. Figure 10c displays the posterior mean for $\rho(x)$ given the one million observations depicted in 10b. Figure 10d shows the posterior uncertainty (one standard deviation) about the estimated mean. The million-observation model recovers the true latent function well.

Figure 11 summarizes predictive quality of ZIGGY as a function of data set size on held out test data using RMSE and LL. This illustrates the benefit of including more training data — root mean squared error (RMSE) decreases (and log likelihood increases) significantly as data set size grows. For example, the RMSE for $N = 100,000$ is 2.6 times bigger than the RMSE for $N = 1,000,000$, (.082 vs. .031) and the average log likelihood is significantly better for the million-observation model.

Figure 12 makes a more direct graphical comparison of the posterior estimate of the latent function as we increase data set size N . As we incorporate more data into the nonparametric model, the form of the true underlying function emerges. To accurately visualize and interpret large scale features of the latent dust distribution, we will want to incorporate as many stellar observations as possible.

F.2 Comparing kernels

We compared multiple models by fitting the variational approximation and tuning the covariance function parameters for five different kernel choices. In this synthetic setup, we ran each model for 50 epochs, saving the the model with the best ELBO value. We used mini-batches of size $|B| = 1,000$, and started the step size at .1, reducing it every epoch by multiplying by a decay factor of .95.

For kernels that do not have a closed form semi-integrated version, we used $L = 30$ uniform grid Monte Carlo samples to estimate the integrated covariance. We chose this on the conservative end — in Appendix E.1 shows that on the order of $L = 10$ to 20 samples is often just as effective as the analytic kernel in the squared exponential case.

We validate the inferences against a set of 2,000 held-out test observations, which include ground truth extinctions e_* and pointwise values, ρ_* . We quantify the quality of the inferences with mean squared error, log likelihood, and the χ^2 -statistic on the test data. We also visually

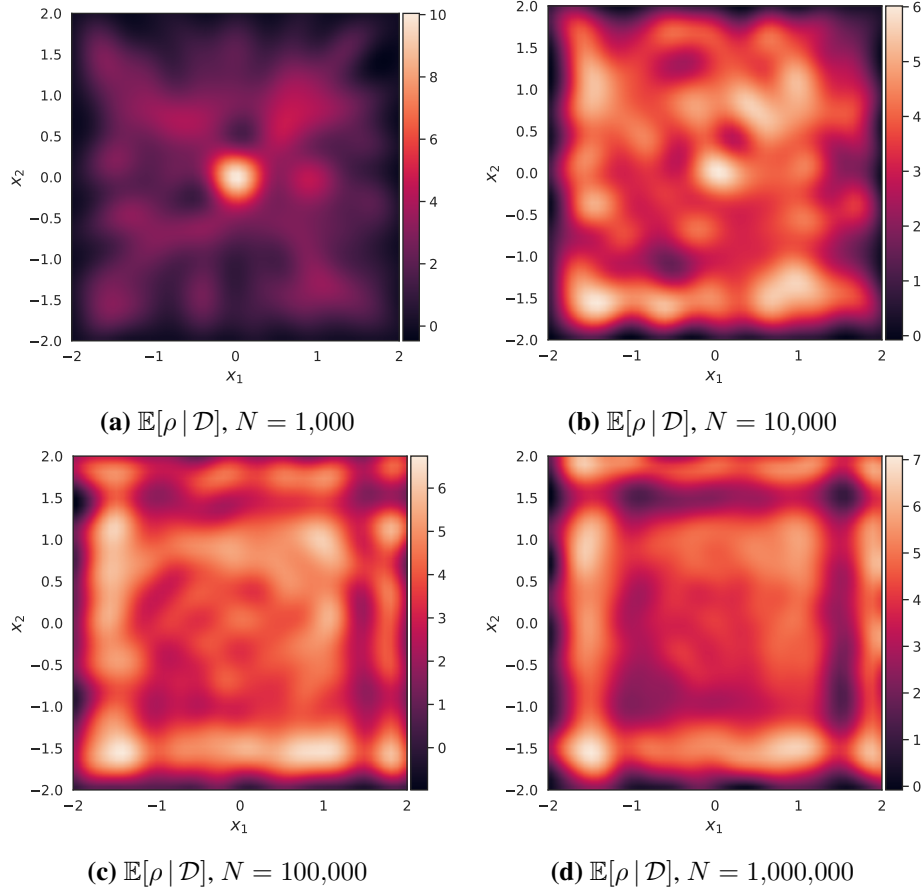


Figure 12: More data leads to more accurate function posterior predictions.

validate ZIGGY with a QQ -plot and coverage comparison, also on test data. We also visualize the behavior ZIGGY as a function of distance to the origin — specifically, we visualize how accurate and well-calibrated test inferences are as synthetic observations are made farther away.

In Figure 13 we compare the mean squared error (MSE), the log likelihood, and the χ^2 statistic on the held out test data. We compare five different kernels – (i) Gneiting $\alpha = 1$, (ii-iv) Matérn, $\nu \in \{1/2, 3/2, 5/2\}$, and (v) the squared exponential kernel. The results match our expectations. The true $\rho(\cdot)$ is smooth, and the smoother kernels tend to have lower predictive error, higher log likelihood, and better calibrated χ^2 statistic (closer to one). The test statistic comparison has chosen a good match in the squared exponential kernel.

We also note that the MSE for the process evaluations ρ_* is much higher than the test MSE for extinctions e_* . This is also expected — intuitively, if the $\rho(\cdot)$ predictions are well-calibrated, then over a larger distance the pointwise errors can be averaged out, resulting in a better predictor for extinctions.

A crucial property of a good posterior approximation is well-calibrated uncertainty. To evaluate the quality of the uncertainty measurements for unobserved extinctions and pointwise process values, we inspect statistics of test-sample z -scores

$$z_* = \frac{e_* - \mathbb{E}[e_* | x_*, \mathcal{D}]}{\sqrt{\mathbb{V}[e_* | x_*, \mathcal{D}]}} \quad (88)$$

for both e_* and ρ_* . If the predictions are well-calibrated, the statistics of predictive z -scores

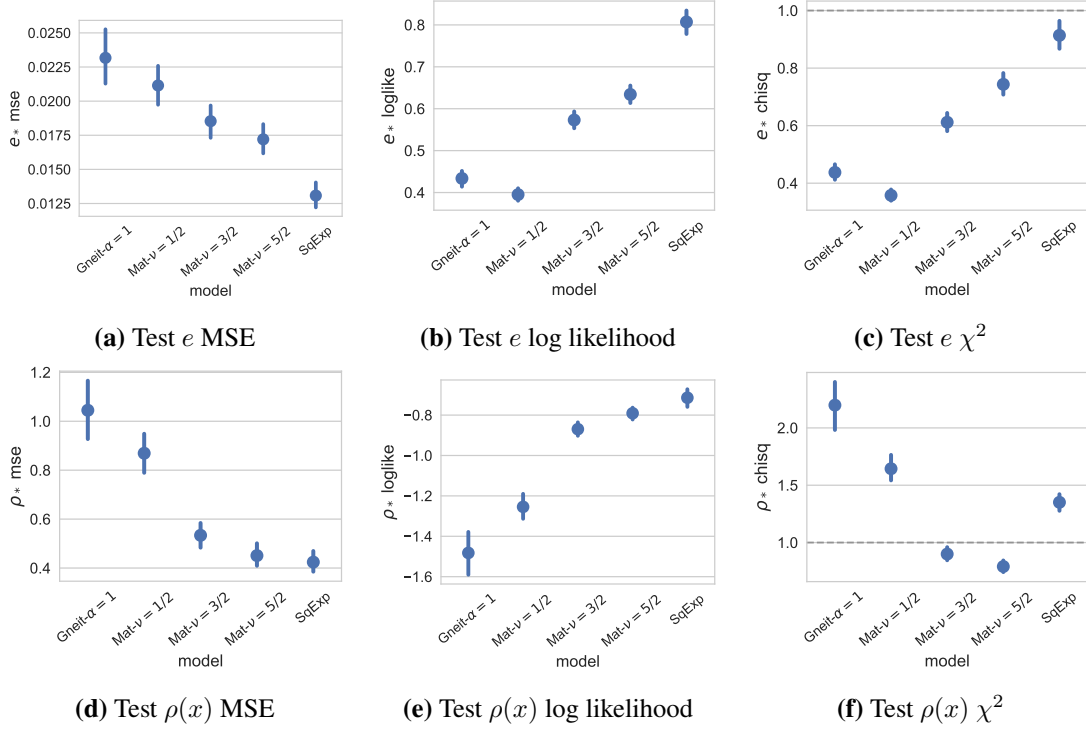


Figure 13: Predictive summaries across different models and inference schemes.

should resemble a standard normal distribution. Concretely, the order statistics of a collection of N_{test} z -scores should closely match the theoretical quantiles of a standard normal distribution — a relationship that can be graphically inspected with a QQ-plot. To compare different models, we visualize QQ-plots for the different covariance functions in Figure 14. As an additional summary of calibration, we compare the fraction of predicted examples covered by 1/2, 1, 2, and 3 posterior standard deviations, summarized in Table 2. We see that the squared exponential kernel z -scores and empirical coverage are not far from what is expected by a theoretical standard normal distribution, indicating that the estimates are well-calibrated.

We also depict model fit statistics as a function of distance from the origin in Figure 15. In Figures 15a and 15b show that pointwise predictions are again well-calibrated as a function of distance, though we observe a small amount of concentration about 0 for the extinction predictions. This indicates that the predictive model was too conservative, or not confident enough in the posterior expectation at nearby values. This is corroborated by Figure 15c, which shows the posterior variance for extinctions is high at nearby (and distant) values, however MSE are high mostly for distant values. Good calibration, even at far distances, is encouraging, as the goal is to form good estimates of this density far away from the observer location.

G Additional Synthetic Experiments

In this supplemental section, we examine the effect of hyper parameter choices on algorithm performance. Specifically, we study two choices: (i) the whitened and standard parameterizations and (ii) the effect of the Monte Carlo semi-integrated covariance estimator on stochastic variational inference.

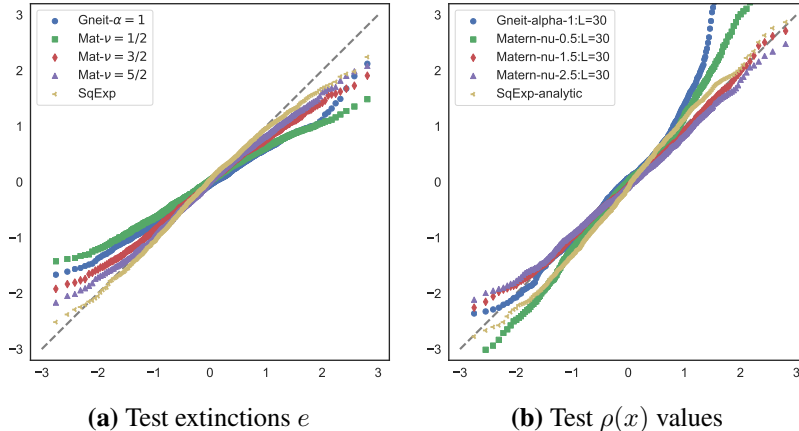


Figure 14: Posterior for extinctions e and dust density ρ are well calibrated. QQ-plot for predicted distributions on 2,000 held out integrated- ρ test points e_* . Theoretical normal quantiles are on the horizontal axis, and predictive z -scored quantiles are on the vertical axis.

	Gneit- $\alpha = 1$	Mat- $\nu = 1/2$	Mat- $\nu = 3/2$	Mat- $\nu = 5/2$	SqExp	$\mathcal{N}(0, 1)$
σ						
0.5	0.536	0.560	0.441	0.407	0.384	0.383
1.0	0.880	0.917	0.785	0.730	0.679	0.683
2.0	0.997	0.999	0.999	0.988	0.971	0.955
3.0	1.000	1.000	1.000	1.000	1.000	0.997

Table 2: Coverage fractions at various levels of z -score standard deviation σ for test extinctions e_* . Relative to theoretical coverage fractions, the inferences concentrate too many predictions near zero — a sign that we are not confident enough.

G.1 Algorithm experiments

The inference algorithm developed in Section 4 involves two key choices, optimizing in the whitened space and the number of Monte Carlo samples used to approximate the semi-integrated kernel. To validate our choices, we investigate the impact of these choices on the inference algorithm and predictions. For simplicity, we assume the number and position of inducing points is fixed.

Whitened parameterization comparison We compare the optimization performance of the two parameterizations detailed above: (i) the *standard* parameterization of variational parameters \mathbf{m} , \mathbf{S} and covariance function parameters θ ; and (ii) the *whitened* parameterization of variational parameters $\tilde{\mathbf{m}}$, $\tilde{\mathbf{S}}$ and covariance function parameters θ .

We fit the above synthetic dataset with $N = 5,000$ observations using stochastic gradient optimization with batches of size 1,000, for 10 epochs. We fix the learning rate for the variational parameters, and we vary the learning rate for the covariance function parameters to be $\Delta \in [1e-4, 1e-5, 1e-6]$. We also vary the initial value of σ^2 to be in $\sigma_0^2 \in [1, 10, 100, 1,000]$. We fit 24 models, 12 standard and 12 whitened.

We compare the mean squared errors for the test e and $\rho(x)$ values in Figure 16, showing that the models fit in the whitened space have lower mean squared errors. Empirically, we also find that optimizing in the whitened space leads to better predictions in fewer epochs.

Semi-Integrated Estimators Additionally, we examine the affect of the number of Monte

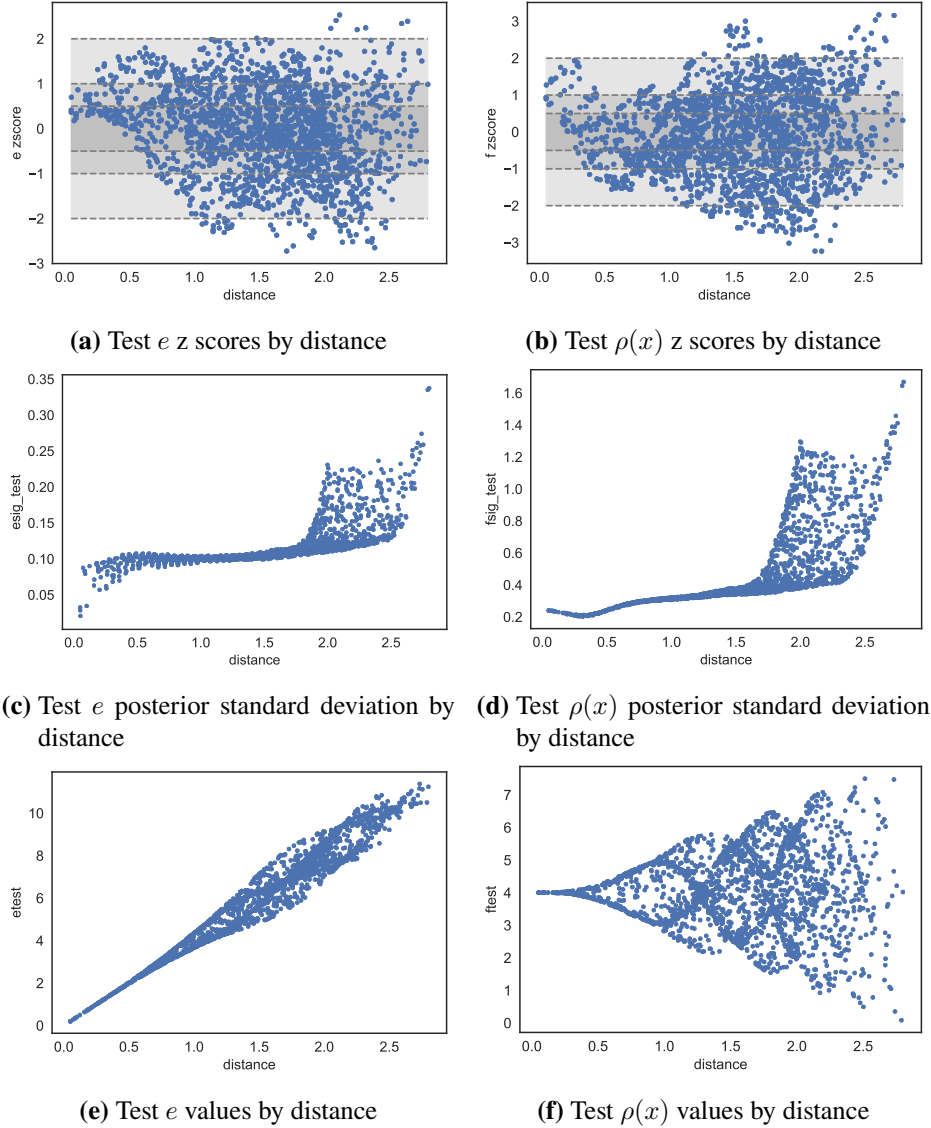


Figure 15: Posterior summaries as a function of distance to the origin (observation point).

Carlo samples used to estimate the semi-integrated covariance function, L . We leverage the fact that the squared exponential kernel admits a closed form semi-integrated covariance function so we can directly compare Monte Carlo estimators with different sample sizes L to the analytic version. Further, we use the analytic form of the semi-integrated covariance function to compute the true variational objective for all approaches; this true objective value is unavailable when the semi-integrated covariance function is unavailable. Figure 9 compares optimization traces of the variational objective using different values of L , ranging from 5 to 50. We see that the performance of the Monte Carlo gradients with $L = 20$ closely mimics the model fit with the exact gradient. We use $L = 30$ when optimizing with the Gneiting and Matérn covariance functions to be conservative.

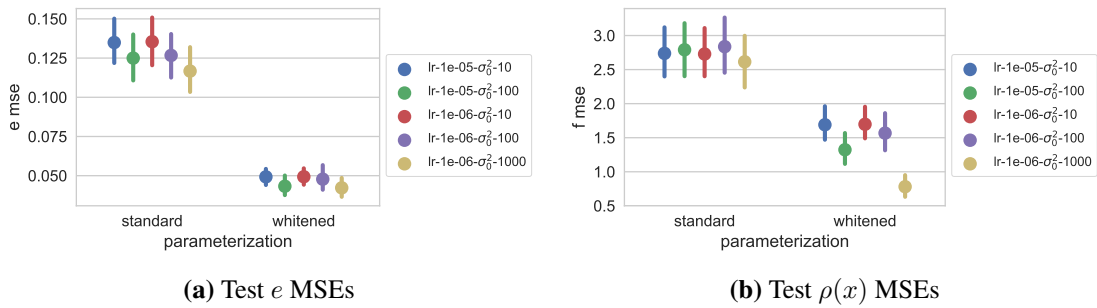


Figure 16: Optimizing with the whitened parameterization leads to better predictions. We ran stochastic optimization initialized at many different initial settings (the top five shown above) for ten epochs. The resulting predictive mean squared error for integrated values e (left) and pointwise values $\rho(x)$ (right) are plotted above. Optimizing in the whitened space dramatically improves predictive accuracy.